

## SPHEREx 0.75 to 5 $\mu\text{m}$ Spectra for a Sequence of Nearby Brown Dwarfs

ZAFAR RUSTAMKULOV,<sup>1</sup> J. DAVY KIRKPATRICK,<sup>1</sup> RACHEL AKESON,<sup>1</sup> MICHAEL W. WERNER,<sup>2</sup> MATTHEW L. N. ASHBY,<sup>3</sup>  
TZU-CHING CHANG,<sup>2,4</sup> SHUANG-SHUANG CHEN,<sup>4</sup> ASANTHA COORAY,<sup>5</sup> BRENDAN P. CRILL,<sup>2,4</sup> OLIVIER DORÉ,<sup>2,4</sup>  
C. DARREN DOWELL,<sup>2,4</sup> ANDREAS L. FAISST,<sup>1</sup> HOWARD HUI,<sup>4,2</sup> WOONG-SEOB JEONG,<sup>6</sup> MIJU KANG,<sup>6</sup> PHIL M. KORNGUT,<sup>4</sup>  
CAREY M. LISSE,<sup>7,8</sup> DANIEL C. MASTERS,<sup>1</sup> GARY J. MELNICK,<sup>3</sup> CHI H. NGUYEN,<sup>4</sup> ROBERTA PALADINI,<sup>1</sup> VOLKER TOLLS,<sup>3</sup>  
YUJIN YANG,<sup>6</sup> AND MICHAEL ZEMCOV,<sup>9,2</sup>

<sup>1</sup>*IPAC, California Institute of Technology, MC 100-22, 1200 E California Blvd, Pasadena, CA 91125, USA*

<sup>2</sup>*Jet Propulsion Laboratory, California Institute of Technology, 4800 Oak Grove Drive, Pasadena, CA 91109, USA*

<sup>3</sup>*Center for Astrophysics | Harvard & Smithsonian, Optical and Infrared Astronomy Division, Cambridge, MA 02138, USA*

<sup>4</sup>*Department of Physics, California Institute of Technology, 1200 E. California Boulevard, Pasadena, CA 91125, USA*

<sup>5</sup>*Department of Physics & Astronomy, University of California Irvine, Irvine, CA 92697, USA*

<sup>6</sup>*Korea Astronomy and Space Science Institute (KASI), 776 Daedeok-daero, Yuseong-gu, Daejeon 34055, Republic of Korea*

<sup>7</sup>*Johns Hopkins University, 3400 N Charles St, Baltimore, MD 21218, USA*

<sup>8</sup>*Johns Hopkins University Applied Physics Laboratory, Laurel, MD 20723, USA*

<sup>9</sup>*School of Physics and Astronomy, Rochester Institute of Technology, 1 Lomb Memorial Dr., Rochester, NY 14623, USA*

### ABSTRACT

The SPHEREx all-sky survey has now measured the R $\sim$ 40-100 infrared spectra of thousands of nearby brown dwarfs in the chemically rich 0.75-5  $\mu\text{m}$  range. The survey's wide spectral coverage and high S/N permits flux measurements that capture several broadband molecular absorption features, and upwards of 80% of the total bolometric luminosity of most brown dwarfs. Atmospheric models are known to yield systematic disagreements in the inferred temperatures and radii of brown dwarfs, necessitating benchmarking against observations. In this work, we present SPHEREx spectra across a broad sequence of 37 nearby field brown dwarfs, ranging from L0 to Y4 ( $\sim$ 2500-250 K) and compare them to theoretical expectations. We additionally compile spectra for separate low-gravity and low-metallicity objects, and show how they trend with constant spectral type. We fit the measured spectra to the well-known forward model grids Sonora Diamondback, Elf Owl, BT-Settl, ATMO2020 and ATMO2020++ and compare their goodness-of-fit as a function of wavelength, spectral type, and treatment of clouds and chemistry. We find that the models continue to struggle to simultaneously fit the J/H/K peaks and the 4  $\mu\text{m}$  opacity window, especially in L/T transition objects. The largest deviations appear around the chemistry-sensitive CO<sub>2</sub> and CO features. Despite these offsets, the models broadly capture their trends across the L/T transition, with the observed sample of field dwarfs strongly preferring the weak vertical mixing ( $k_{zz} = 10^4 \text{ cm}^2\text{s}^{-1}$ ) Elf Owl models over strong mixing. The spectra shown here along with future SPHEREx data will help guide improvements to models.

*Keywords:* Brown dwarfs (185), L dwarfs (894), T dwarfs (1679), Y dwarfs (1827), Sky surveys (1464), Infrared spectroscopy (2285), Stellar atmospheres (1584)

### 1. INTRODUCTION

Brown dwarfs, substellar objects not massive enough to sustain stable hydrogen fusion, are an exceptionally colorful and varied group of celestial bodies. Among the  $\sim$ 10,000 known brown dwarfs (J. Gagné et al. 2026), effective temperatures span 250 to 2,500 K while intrinsic

luminosities range over four orders of magnitude depending on mass and age (e.g., A. Sanghi et al. 2023). The vertically thin photosphere of a brown dwarf is the ultimate mediator of its interior heat flux and therefore controls its radius evolution. Unlike stars, brown dwarfs cool, contract, and spin up with age (e.g., A. C. Schneider et al. 2018; J. M. Vos et al. 2020), resulting in observable population-wide changes in the character of their clouds and chemistry. In this way, their molecu-

rich spectra tell stories of the delicate couplings linking their atmosphere, weather, climate, and interior through time.

Compositional trends in brown dwarf atmospheres resemble those of irradiated gas giant exoplanets—the hottest objects show strong H<sub>2</sub>O, CO, and alkali opacity, with magnesium silicate clouds appearing, then sinking below the photosphere as they cool below  $\sim 1400$  K with age (e.g., P. Gao et al. 2020; G. Suárez & S. Metchev 2022; J. D. Lothringer et al. 2026). At colder temperatures and older ages, sulfide and chloride cloud species appear as CH<sub>4</sub> becomes chemically favored over CO below  $\sim 1000$  K in T dwarf atmospheres (e.g., K. Lodders & B. Fegley 2002; M. E. Tannock et al. 2022; A. J. Burgasser et al. 2025). The coldest brown dwarfs, the Y dwarfs, begin to resemble Jupiter and Saturn, whose CH<sub>4</sub> and NH<sub>3</sub>-dominated atmospheres have vertically stratified clouds of diverse compositions, and with trace quantities of H<sub>2</sub>S and PH<sub>3</sub> (S. A. Beiler et al. 2024; H. Kothari et al. 2024). These objects show diversity in composition and cloud coverage (e.g., A. Lueber et al. 2026). Unlike mature giant planets and exoplanets, unbound field brown dwarf atmospheres are heated entirely from within. By virtue of their independent thermochemical evolution, field brown dwarfs represent an idealized glimpse into the interacting processes liberating their primordial heat. Yet despite being internally heated, some brown dwarfs exhibit heat sources of uncertain origin manifesting as mysterious thermal inversions, or stratospheres, and chromospheric activity (e.g., J. K. Faherty et al. 2024; A. Reiners & G. Basri 2008). Oddities aside, the bulk of brown dwarf fundamental parameters can only be estimated from model fits to their spectra. Namely, for an isolated self-luminous field dwarf, the radius, temperature, and mass estimates rely on the information content encoded by theoretical atmosphere models (A. Burrows et al. 2001; I. Baraffe et al. 2003; D. Saumon & M. S. Marley 2008; M. S. Marley et al. 2021). To constrain their ages, these fundamental parameters are compared to evolution models that track the temperature and radius for a brown dwarf of given mass (J. C. Filippazzo et al. 2015; T. J. Dupuy & M. C. Liu 2017).

Today, forward models gridded along the axes of temperature and gravity only qualitatively represent the major features seen in spectra, with large,  $\gtrsim 20\%$  systematic differences dependent on the chosen input physics assumptions (e.g., G. Suárez et al. 2021; S. Petrus et al. 2024; Z. Zhang et al. 2021). While theoretical and lab-measured molecular databases have been improving, model substellar spectra still differ from observations due to differences in their handling of clouds, chemistry,

and the thermal profile. Empirical spectral classification continues to be a useful practice to augment these model-dependent determinations by populating a relative scale upon which to compare different objects.

### 1.1. Spectral Classification

In this paper, we present sequences of low-mass, low-temperature spectral standards at Solar age/composition, at lower gravities, and at subsolar metallicities. As explained in J. D. Kirkpatrick (2005), spectral types for these objects follow the form {metallicity class}+{temperature class}+{gravity class}, where

$$\begin{aligned} \text{metallicity class} &\in \{\text{d, sd, esd, usd}\}^{10} \\ \text{temperature class} &\in \{\text{Mn, Ln, Tn, Yn}\}^{11} \\ \text{gravity class} &\in \{\alpha, \beta, \gamma, \delta\}^{12} \end{aligned}$$

For the metallicity classes, d = dwarf, sd = subdwarf, esd = extreme subdwarf, and usd = ultra subdwarf. For the gravity classes,  $\alpha$  = field age and field gravity, with  $\beta$ ,  $\gamma$ , and  $\delta$  marking objects with progressively lower gravities and younger ages (K. L. Cruz et al. 2009). The  $n$  under temperature class is a gradation that generally ranges from 0 to 9.5 except for the Y dwarfs, for which the range currently runs only from 0 to 2.

For example, a normal field early-L dwarf might have a full spectral type of dL0 $\alpha$ ; however, the d prefix and  $\alpha$  suffix are almost never appended for these Solar-composition and Solar-age objects so that the type can be written more simply as L0. A late-M subdwarf, which can be interpreted as an old object with subsolar metallicity, might be denoted by sdM9. An even lower metallicity late-T extreme subdwarf would be denoted as esdT8, and an even lower metallicity early-Y ultra subdwarf denoted as usdY0. Likewise, a solar-composition

<sup>10</sup> For late-M to mid-L dwarfs, these correspond very roughly to values of  $[Fe/H] \approx 0.0$ ,  $-1.0 < [Fe/H] < 0.0$ ,  $-1.7 < [Fe/H] < -1.0$ , and  $-2.3 < [Fe/H] < -1.7$ , respectively (Figure 21 of Z. H. Zhang et al. 2017). The corresponding metallicity ranges for T and Y subdwarfs have yet to be determined due to the rarity of these objects in current samples.

<sup>11</sup> These correspond roughly to  $T_{eff}$  ranges of 3800-2250K, 2250-1250K, 1250-450K, and  $< 450$ K, respectively (Figure 9.19 of R. O. Gray & C. Corbally 2009 and Figure 22b of J. D. Kirkpatrick et al. 2021.)

<sup>12</sup> These are believed to correspond roughly to age ranges of  $> 1$  Gyr,  $\sim 100$  Myr,  $\sim 10$  Myr, and  $\sim 1$  Myr, respectively (Section 5.2 of J. D. Kirkpatrick 2005). If we consider the range from the M/L dwarf boundary down to the T/Y dwarf boundary, the models of A. Burrows et al. (1997) suggest that these gravity designations correspond to overlapping ranges of  $5.4 < \log(g) < 4.4$  for  $\alpha$ ,  $5.2 < \log(g) < 4.0$  for  $\beta$ ,  $4.8 < \log(g) < 3.8$  for  $\gamma$ , and  $4.3 < \log(g) < 3.4$  for  $\delta$ , with the exact gravity value depending upon the object's temperature class.

early-L exhibiting mild effects of lower gravity – generally interpreted as a sign of youth, as these objects have not yet contracted to their final equilibrium radii – might be denoted as L2 $\beta$ . An even lower gravity and possibly even younger late-M-type brown dwarf might be denoted as M8 $\gamma$ , and an even lower gravity and possibly even younger mid-T denoted as T5 $\delta$ .

Late-M, L, T, and Y dwarf spectral standards were taken from several sources. Standards with typical field age and field composition were taken from J. D. Kirkpatrick et al. (2010), who drew from late-M and L primary and secondary standards first established at optical wavelengths by P. C. Boeshaar & J. A. Tyson (1985), J. D. Kirkpatrick et al. (1991), and J. D. Kirkpatrick et al. (1999) and further drew from T dwarf spectral standards established in the near-infrared by A. J. Burgasser et al. (2006). The latter reference reached as cold as spectral type T8, but later near-infrared standards at types  $\geq$ T9 were proposed by M. C. Cushing et al. (2011) and J. D. Kirkpatrick et al. (2012).

Standards at low gravity were taken from the lists of K. L. Cruz et al. (2009), and those at low metallicity were drawn from the lists of S. Lépine et al. (2007) and Z. H. Zhang et al. (2017).

### 1.2. Brown Dwarf Atmosphere Panorama

The 0.75-5.0  $\mu$ m SPHEREx spectra of brown dwarfs have many features that can be used to study the physical and chemical conditions of their atmospheres. The H<sub>2</sub>O and CH<sub>4</sub> absorption band strengths are a direct probe of temperature (K. Lodders & B. Fegley 2002; J. D. Kirkpatrick et al. 2010). Carbon tracers – CH<sub>4</sub>, CO<sub>2</sub>, and CO – are thought to provide clues about vertical mixing and disequilibrium chemistry (H. Kothari et al. 2024); the C/O ratio itself is believed to hold clues about the brown dwarf’s formation pathway (M. W. Phillips et al. 2024). The main tracer of nitrogen – NH<sub>3</sub> – can independently be used to study vertical mixing, although its presence is dwarfed by overlying bands of H<sub>2</sub>O and CH<sub>4</sub> (D. Saumon et al. 2006; M. C. Cushing et al. 2011), and is unlikely to be detectable with SPHEREx. Another strong absorber is collision-induced absorption (CIA) by H<sub>2</sub> centered at 2.1  $\mu$ m (A. Borysow 2002), whose broad pressure-sensitive continuum opacity is a probe of the depth of the photosphere (D. Saumon et al. 1994). Figure 1 shows a representative SPHEREx spectrum with prominent features shaded by the dominant molecular opacity source at a given wavelength. The opacities are taken from the compiled PICASO opacity database (N. E. Batalha et al. 2019, and references therein). The spectrum is dominated by H<sub>2</sub>O, the main oxygen tracer, and CH<sub>4</sub> up to the opacity

window at 4.2  $\mu$ m, beyond which CO<sub>2</sub> and CO become prominent.

### 1.3. SPHEREx

SPHEREx<sup>13</sup>, the Spectro-Photometer for the History of the Universe, Epoch of Reionization, and Ices Explorer (J. J. Bock et al. 2025), is a NASA medium explorer mission which has been in science operations since 1 May, 2025. SPHEREx is conducting an all-sky near-infrared spectral survey in 102 spectral channels spanning from 0.75 to 5  $\mu$ m with spectral resolution of  $\sim$ 40 shortward of 4  $\mu$ m and  $\sim$ 120 from 4 to 5  $\mu$ m. SPHEREx will survey the whole sky 4 times during its 25 month prime mission. In addition, SPHEREx observes deep fields in the north and south ecliptic poles, where sources are observed up to hundreds of times per spectral channel. The SPHEREx Science Team goals, from cosmology to ices in the Milky Way, are described in J. J. Bock et al. (2025). In the SPHEREx instrument, the focal plane is organized into two sides, both of which include 3 $\times$ 1 H2RG detector arrays (Korngut, P. et al. 2026). Each detector has been overlaid with a linear variable filter, providing sensitivity to a specific wavelength band, and covers 3.5 $\times$ 3.5 degrees on the sky with 6''15 pixels. The SPHEREx observations are a unique all-sky data set that is available at the NASA/IPAC Infrared Science Archive (IRSA)<sup>14</sup>.

### 1.4. Motivation

Before SPHEREx, survey characterization of brown dwarf atmospheres was largely enabled by the broadband near-infrared magnitudes from 2MASS  $J, H, K_s$  at 1.1-1.36, 1.5-1.8, and 2-2.4  $\mu$ m, with 5 $\sigma$  depths of  $J, H, K_s \simeq 17.4, 17.2, 16.9$  AB mag, and from WISE/AllWISE  $W1, W2$  at 2.8–3.9  $\mu$ m and 4–5.2  $\mu$ m, with 5 $\sigma$  depths of  $W1, W2 \simeq 19.6, 19.3$  AB mag (M. F. Skrutskie et al. 2006; E. L. Wright et al. 2010). The combined 2MASS+WISE broadband SED therefore samples brown dwarfs at an effective photometric resolving power of only  $R \sim 5-8$ . In comparison, SPHEREx achieves 5 $\sigma$  per-exposure depths of  $\sim$ 19.5 in the 0.7-3.8  $\mu$ m range with  $R \sim 40$ , and  $\sim$ 17.5-18.5 AB mag depths in the 3.8-5  $\mu$ m range with  $R \sim 110$ .

With their higher sensitivity, increased spectral resolution, and wide wavelength grasp, SPHEREx spectra are uniquely well-suited for detailed atmospheric characterization of nearby brown dwarfs (2-30 pc, see Table 1). For these reasons, the SPHEREx spectral atlas represents the frontier of brown dwarf survey science. In

<sup>13</sup> <https://spherex.caltech.edu>

<sup>14</sup> <https://irsa.ipac.caltech.edu>

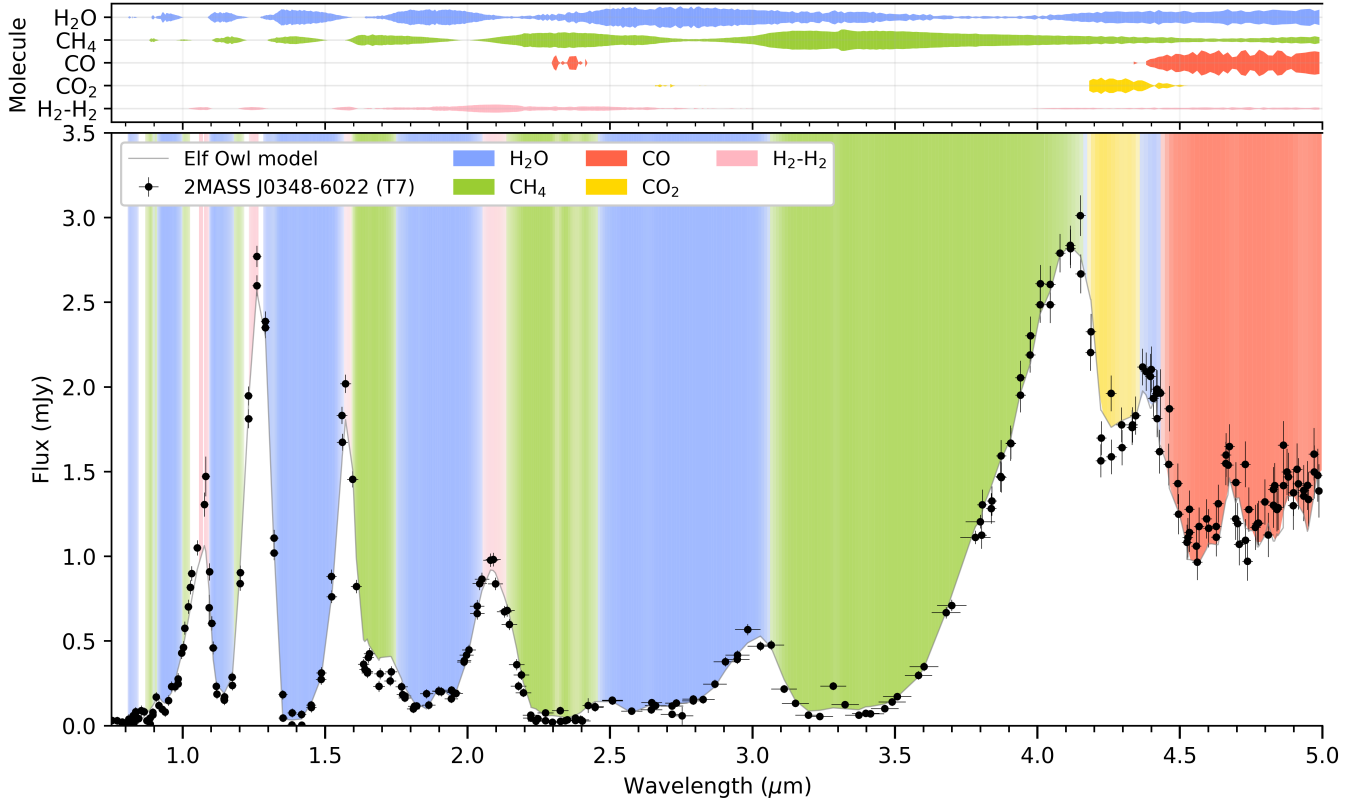


**Figure 1.** The SPHEREx spectrum of the typical T7 field dwarf 2MASS J03480772-6022270 overplotted with a map of the key molecular opacity contributors and the best-fitting Sonora Elf Owl model. The widths of the shaded regions in the top panel are proportional to the log of the opacity of each molecule. The corresponding shaded regions in the bottom panel highlight the dominant absorber at a given wavelength. The spectrum is dominated by alternating and overlapping bands of water and methane, with carbon dioxide and carbon monoxide appearing at redder wavelengths. There is a newly-apparent weak CH<sub>4</sub> emission feature at 3.3  $\mu\text{m}$ , possibly resulting from a thermal inversion (e.g., J. K. Faherty et al. 2024)

particular, the poorly studied 3–5  $\mu\text{m}$  range encapsulates the main opacity features of CH<sub>4</sub>, CO<sub>2</sub>, and CO. These species are sensitive diagnostics of thermochemistry and composition, and so far only a handful of brown dwarfs have been observed at these wavelengths with JWST and AKARI. SPHEREx has now gathered the spectra of thousands of brown dwarfs (e.g., J. Gagné et al. 2026), with many new discoveries readily possible.

Another important and surprising application of SPHEREx spectra is in cosmology, where Y-dwarfs can be mistaken for high-redshift galaxies due to their similar magnitudes and infrared colors. A recent such case of mistaken identity was pointed out in M. Bradač et al. (2026), where two high-redshift galaxy candidates turned out to be faint, distant brown dwarfs. Thanks to SPHEREx spectra, many instances of such contamination in galaxy surveys can be cleared up by comparing the object’s spectrum to representative templates. Conversely, these spectra may help identify extremely distant brown dwarfs in our galaxy in future surveys.

In this work, we present a curated sample of high-S/N SPHEREx spectra across the full gamut of brown dwarf temperature, gravity, and metallicity to directly compare state-of-the-art theoretical model grids, with the motivation of distilling the most relevant physics to inform the models’ continued improvement. Given that field brown dwarfs are in some ways simpler to model and observe than transiting exoplanets, adequately fitting their observables is imperative to improving the characterization of Jovian and lower mass worlds.

## 2. OBSERVATIONS AND DATA ANALYSIS

### 2.1. SPHEREx Pipeline

The SPHEREx science data processing occurs at the SPHEREx Science Data Center (SSDC) at Caltech/IPAC and by the SPHEREx Science Team. The SSDC performs the first three levels of processing, including astrometric and photometric calibrations, while the Science Team produces higher-level image and catalog products. The SSDC pipeline infrastructure is described in R. Akeson et al. (2025) and the individual pipeline

modules are documented in the SPHEREx Explanatory Supplement<sup>15</sup> at IRSA.

For this work, we use calibrated Level-2 spectral image files from IRSA, with calibration version QR2. Given the sampling strategy employed by SPHEREx (S. Bryan et al. 2025), the exact spectral sampling is not uniform for each source. These calibrated images are the input for the Spectrophotometry Tool, one of the SPHEREx tools hosted by IRSA. This tool performs photometric measurements of selected sources using position and morphology information provided by the user. Here, we used proper motion corrected positions, specified that all sources are point-like, and used the tool version with the corrected point-spread function (PSF) (as of April 2026). The tool algorithm is based on the community software package Tractor<sup>16</sup>, which uses generative modeling of astronomical images to measure a maximum likelihood solution (Section 3.3 of the Explanatory Supplement). A local background is also calculated and subtracted. If the local region does not contain a sufficient number of unflagged pixels, a global solution is used. In addition to the source flux and uncertainty, a per point fit quality metric is calculated and flags from the image are propagated to the output. The spectra have spectral flux density units,  $F_\nu$ , in Jy. At the time of writing, the spectral absolute gain calibration of SPHEREx has a quoted reliability of  $\lesssim 3\%$  for Bands 1-4, and  $\lesssim 5\%$  for Bands 5 and 6 in the QR2 data, which are used in this work. The gain calibration is currently being refined to a higher accuracy and reliability in Ashby, M., et al. (2026).

### 2.2. Target Selection Caveats

The low-gravity and low-metallicity sequences discussed in § 3 below (Table 1) are sourced entirely from the list of standards discussed in § 1.1. Some of the standards for the Solar-age, Solar-metallicity sequence, however, have low S/N compared to other field dwarfs of the same type, have a relatively low number of measurements, or are known binaries, so we have chosen a replacement with the same optical and/or near-infrared spectral type from the 20-pc census of J. D. Kirkpatrick et al. (2024) (see Table 1). A few other standards were excluded because their PSF shapes were extended in WCS-aligned and stacked SPHEREx images compared to the SPHEREx PSF, they have obvious contaminants within 3 pixels of their centroid position, or they are known to be currently contaminated by a background

object based on their proper motion trajectories (as seen in WiseView imagery<sup>17</sup>; D. Caselden et al. 2018). Unlike the spectral standards, these 20-parsec objects should not be used as anchors for the MK Process (W. W. Morgan et al. 1943) but should suffice to show the gross changes in spectral morphology through the sequence.

### 2.3. Data Cleaning

As SPHEREx spectrophotometric measurements can sometimes become affected by cosmic rays, satellite streaks, and Solar particle events, we use the bit-wise pixel quality flags from the Spectrophotometry Tool to apply strict quality cuts to the data. All fluxes with any flag listed in Table 9 of the Explanatory Supplement (other than SOURCE) are excluded to conservatively ensure the cleanliness of the spectra. Visual spot-checks suggest that a poor quality flag does not always reflect an anomalous measurement, and some anomalous measurements do not get flagged, meaning that some objects will show occasional spurious fluxes. There is a known under-flagging of bad pixels in the early data releases, which have since been corrected (as of Dec. 2025). The flagging update was not applied retroactively, so at least half of the observations in this work are subject to under-flagging. We remove spurious points by masking fluxes that lie more than  $4\sigma$  away from the smoothed running median of the data.

## 3. SPECTRAL SEQUENCES

In this section, we present our distinct field, low-gravity, and low-metallicity sequences. The field objects are summarized in Table 1, the low-gravity in Table 2, and the low-metallicity in Table 3.

### 3.1. Qualitative Description

The brown dwarf spectral sequence is mostly carved by the temperature-sensitive bands of H<sub>2</sub>O, CH<sub>4</sub>, CO, CO<sub>2</sub>, and the opacity windows between them (Fig. 2). Across the field-type L dwarfs, the onset of CH<sub>4</sub> becomes visually apparent for objects later than L4, appearing initially as a downward concavity from 3-3.6  $\mu\text{m}$ , then completely dominating the blue side of the 4 $\mu\text{m}$  opacity window all the way through the cooler sequence. CH<sub>4</sub> and H<sub>2</sub>O opacity similarly sculpts the shapes of the NIR J/H/K opacity windows, making them sharper at progressively colder temperatures, and introducing a narrow absorption feature at 1.15  $\mu\text{m}$ . When plotted with flux (Jy) on the vertical axis, the relative heights of the J- and K-band peaks (1.3, 2.2  $\mu\text{m}$ ) begin to reverse at the L/T transition, with the K-band peak falling below

<sup>15</sup> <https://irsa.ipac.caltech.edu/data/SPHEREx/docs/SPHEREx.Expsupp-QR.pdf>

<sup>16</sup> <http://thetractor.org>

<sup>17</sup> <http://byw.tools/wiseview>

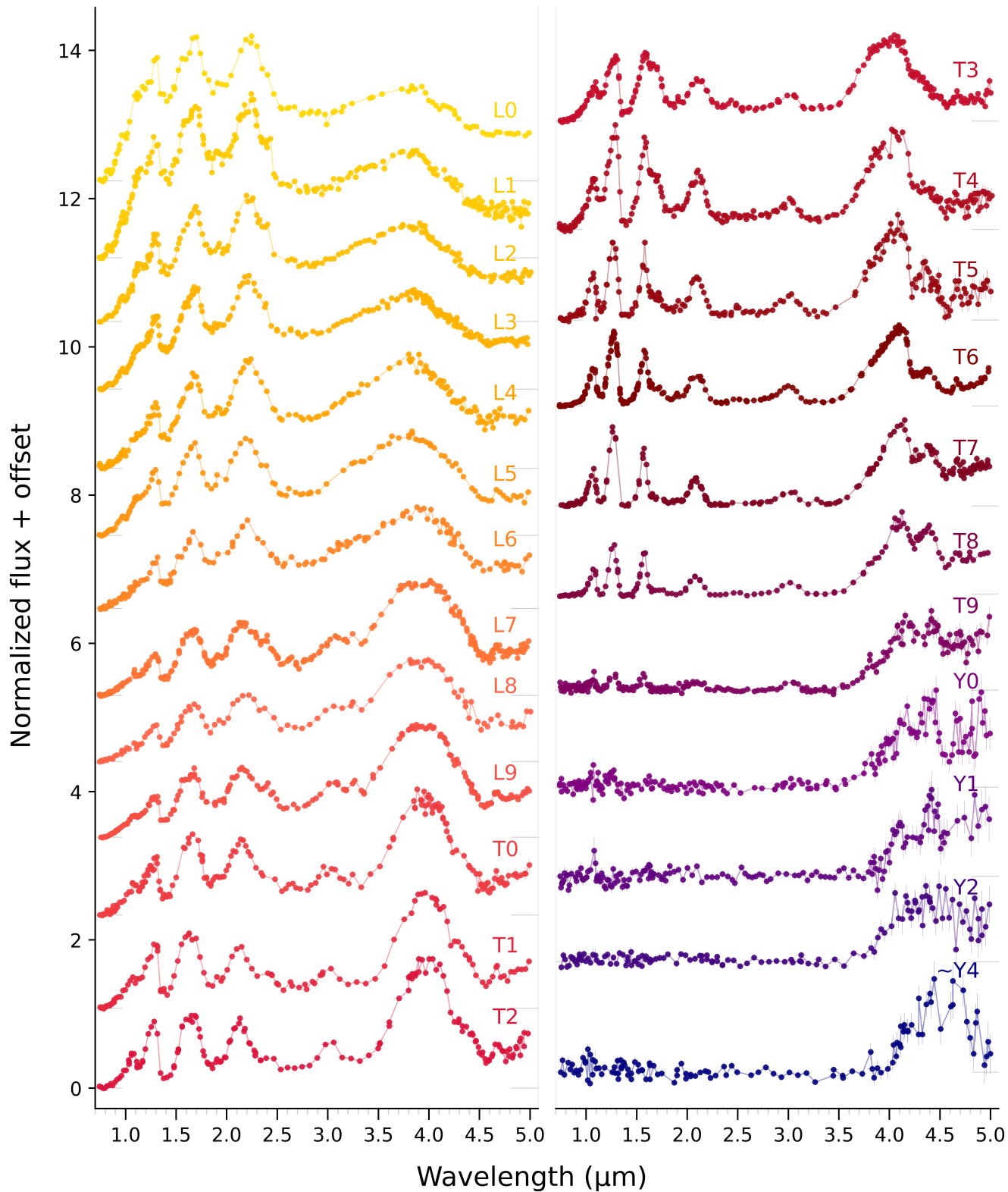


**Figure 2.** The SPHEREx spectral sequence of the field brown dwarfs listed in Table 1. Each spectrum is normalized by the mean of the flux between 3.7 and 4.7  $\mu\text{m}$ , and arbitrarily vertically spaced for visual clarity. The zero-flux level for each spectrum is indicated by the pairs of short grey lines.

**Table 1.** Objects in the spectral sequence of Fig. 2

Spec. Type	Name	Dist. (pc)	Ref.	Standard?	Note
L0	2MASS J17312974+2721233	$11.95 \pm 0.01$	2	No	A
L1	2MASS J21304464-0845205	$26.69 \pm 0.22$	1	Yes	...
L2	2MASS J21041491-1037369	$17.24 \pm 0.08$	2	No	B
L3	2MASS J15065441+1321060	$11.71 \pm 0.03$	2	Yes	...
L4	2MASS J21580457-1550098	$23.20 \pm 0.49$	1	Yes	...
L5	2MASS J15074769-1627386	$7.41 \pm 0.01$	2	No	C
L6	2MASS J10101480-0406499	$17.33 \pm 1.08$	3	Yes	...
L7	2MASS J03400942-6724051	$9.36 \pm 0.04$	2	No	D
L8	2MASS J16322911+1904407	$15.09 \pm 0.37$	4	Yes	...
L9	DENIS J025503.3-470049	$4.87 \pm 0.00$	2	Yes	...
T0	PSO J319.3102-29.6682	$13.14 \pm 0.60$	4	No	...
T1	WISE J124629.65-313934.2	$11.52 \pm 0.20$	2	No	E
T2	2MASS J11220826-3512363	$13.26 \pm 0.28$	2	No	F
T3	PSO J247.3273+03.5932	$12.32 \pm 0.45$	3	No	...
T4	2MASS J22541892+3123498	$13.89 \pm 0.58$	6	Yes	...
T5	WISE J004542.56+361139.1	$17.54 \pm 1.14$	3	No	G
T6	DENIS J081730.0-615520	$5.21 \pm 0.01$	2	No	H
T7	2MASS J03480772-6022270	$8.33 \pm 0.12$	7	No	I
T8	2MASS J04151954-0935066	$5.71 \pm 0.06$	8	Yes	...
T9	WISE J000517.48+373720.5	$7.88 \pm 0.13$	3	No	J
Y0	WISE J205628.91+145953.2	$7.10 \pm 0.10$	3	No	K
Y1	WISE J154151.65-225024.9	$5.99 \pm 0.07$	3	No	L
Y2? <sup>a</sup>	WISE J182831.08+265037.7	$9.97 \pm 0.20$	3	Yes	...
~Y4? <sup>a</sup>	WISE J085510.83-071442.5	$2.28 \pm 0.01$	3	Yes	...

<sup>a</sup>Standards have not yet been established at types later than Y1, so these classifications should be considered tentative.

NOTE— Reference codes for astrometry: (1) Gaia DR3; (2) Gaia EDR3; (3) Kirkpatrick et al. 2021a; (4) Dahn et al. 2017 + CatWISE 2020; (5) Best et al. 2020; (6) Manjavacas et al. 2013 + CatWISE 2020; (7) Kirkpatrick et al. 2019; (8) Dupuy and Liu 2012. Notes: (A) The L0 standard, 2MASS J03454316+2540233, has much lower S/N than the L0 listed. (B) The L2 standard, Kelu-1 AB, is a known binary. (C) The L5 standard, 2MASS J08350622+1953050, has much lower S/N than the L5 listed. (D) The L7 standard, 2MASS J01033203+1935361, has much lower S/N than the L7 listed. (E) The T1 standard, WISE J083717.17-000020.0, has much lower S/N than the T1 chosen. (F) The T2 standard is 2MASS J12545393-0122474. (G) The T5 standard, 2MASS J15031961+2525196, has poorer SPHEREx spectral coverage than the T5 listed. (H) The T6 standard, 2MASS J16241436+0029158, has poorer S/N and spectral coverage than the chosen T6. (I) The T7 standard, 2MASS J07271824+1710012, has poorer spectral coverage than the T7 listed. (J) The T9 standard, UGPS J072227.51-054031.2, has possible contamination in SPHEREx since it lies deep within the Galactic Plane. (K) The Y0 standard, WISE J173835.53+273259.0, has poorer S/N than the Y0 listed. (L) The Y1 standard, WISE J035000.32-565830.2, has poorer S/N than the Y1 listed.

NOTE—The listed spectral types are all near-infrared classifications except for the L3, L6, L8, and T3, whose classifications were done in the optical.

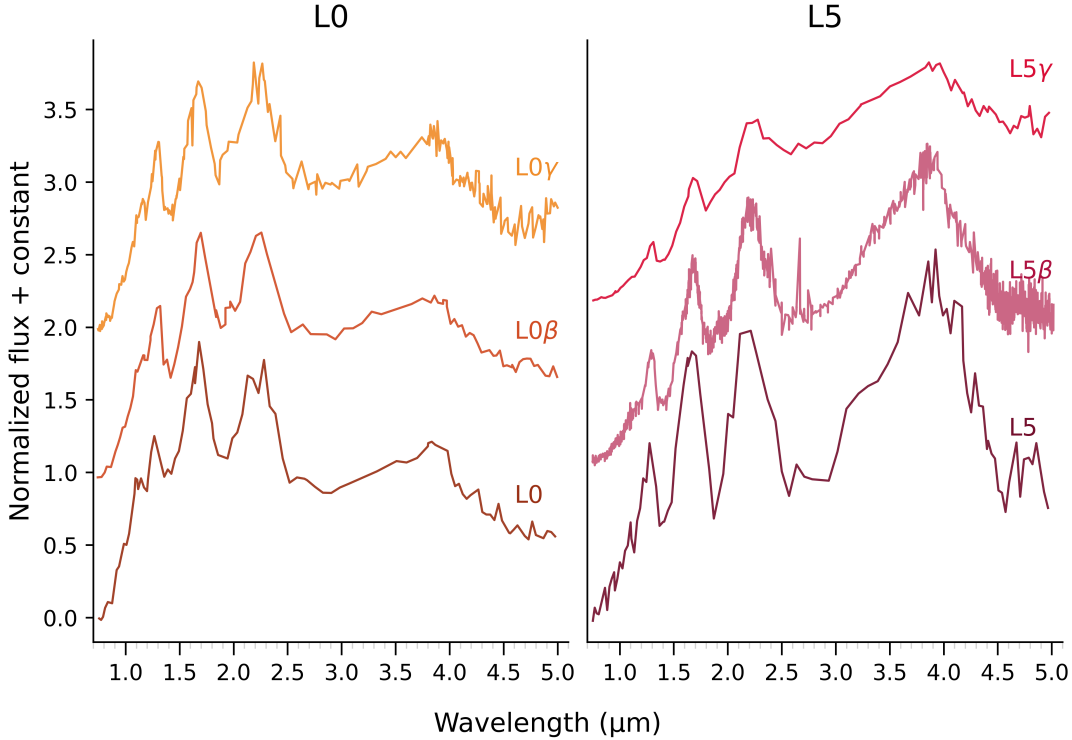


**Figure 3.** The SPHEREx spectral sequence of low gravity brown dwarfs for L0-types (left) and L5-types (right). The lowest-gravity  $\gamma$  types (top) differ from the field-gravity types (bottom) are most distinguished from each other by the relative heights of the NIR peaks, with the K-band peak growing taller relative to the H-band peak with decreasing gravity. For the L5 subtypes, the slope of the 0.7-1.2  $\mu\text{m}$  range and the amplitudes of the water features get weaker with declining gravity, indicative of cloud scattering and isothermality, respectively.

**Table 2.** Low-gravity comparison sequence at L0 and L5.

Spec. Type	Name	Dist. (pc)	Astrometry Ref.	Standard?	Note
L0 $\gamma$	2MASS J00325584-4405058	$34.5 \pm 0.5$	Gaia DR3	Yes	...
L0 $\beta$	2MASS J15525906+2948485	$20.5 \pm 0.07$	Gaia DR3	Yes	...
L0	2MASS J03454316+2540233	$26.4 \pm 0.18$	Gaia DR3	Yes	...
L5 $\gamma$	2MASS J03552337+1133437	$9.16 \pm 0.04$	Gaia EDR3	Yes	...
L5 $\beta$	2MASS J04210718-6306022	$20.0 \pm 1.3$	Kirkpatrick2021a	Yes	...
L5	2MASS J08350622+1953050	$36 \pm 4$	CatWISE2020	Yes	...

NOTE—The low-gravity objects above are as defined by *K. L. Cruz et al. (2009)*. The listed spectral types are all optical classifications except for the L5, whose classification was done in the near infrared.

the H-band peak (1.6  $\mu\text{m}$ ) at subtype T0. The H-band peak eventually becomes shorter than the J-band peak at subtype T4. In the mid-IR,  $\text{CO}_2$  and CO become increasingly apparent beyond subtype L3, with growing absorption notches at 4.15-4.3, and 4.4-4.9  $\mu\text{m}$ , respectively. The fundamental vibration band of the CO band is visible as a subtle peak at 4.67  $\mu\text{m}$  that appears at subtype L4 and persists through the rest of the sequence. The opacity window near 4  $\mu\text{m}$  shifts redward for the

late-T and Y dwarfs due to the saturation of the  $\text{CH}_4$  opacity band, and the declining CO abundance with decreasing temperature. The prominence and sharpness of the 4  $\mu\text{m}$  window peak are maximized at the L/T transition, where  $\text{CH}_4$  and CO opacity together sandwich the peak of the emergent flux.

The low-gravity sequence for subtypes L0 and L5 is shown in Fig. 3. The most noticeable trend with decreasing gravity is the slope from 0.75-1.2  $\mu\text{m}$ ,

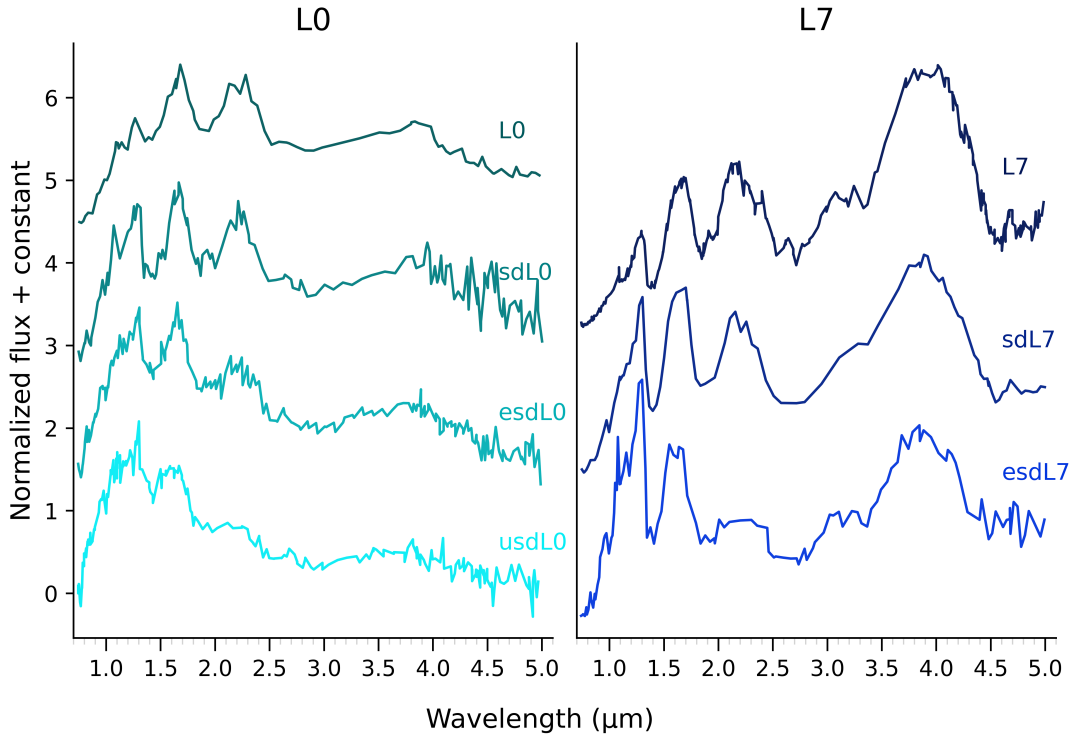


**Figure 4.** The low-metallicity sequence for the L0 and L7 subtype standards. The objects decrease in metallicity from top to bottom. The designations correspond to  $[Fe/H]$  metallicities of  $\approx 0.0$ ,  $-1.0 < [Fe/H] < 0.0$ ,  $-1.7 < [Fe/H] < -1.0$ , and  $-2.3 < [Fe/H] < -1.7$  for the d, sd, esd, and usd L-subtypes, respectively. The decrease in molecular opacity results in a hotter, deeper photosphere, driving an increase in NIR flux, probing deeper where the pressure-broadened  $H_2-H_2$  CIA opacity dominates from 2-3  $\mu m$ .

**Table 3.** Low-metallicity comparison sequence at L0 and L7.

Spec. Type	Name	Dist. (pc)	Astrometry Ref.	Standard?
esdL0	2MASS J00144919-0838207	$50.28 \pm 0.50$	Gaia DR3	Yes
sdL0	2MASS J01301256-1047285	$62.31 \pm 2.62$	Gaia DR3	Yes
L0	2MASS J03454316+2540233	$26.39 \pm 0.18$	Gaia DR3	Yes
usdL0	2MASS J10130734-1356204	$56.47 \pm 0.52$	Gaia DR3	Yes
esdL7	2MASS J05325346+8246465	$24.56 \pm 0.28$	Gaia DR3	Yes
L7	2MASS J03400942-6724051	$9.36 \pm 0.04$	Gaia EDR3	Yes
sdL7	2MASS J14162408+1348263	$9.28 \pm 0.02$	Gaia EDR3	Yes

NOTE—The low-metallicity objects above are as defined by [Z. H. Zhang et al. \(2017\)](#). The listed spectral types are all near-infrared classifications except for the L0, whose classification was done in the optical.

which becomes less steep. The  $L5\gamma$  object 2MASS J08350622+1953050 shows relatively low-amplitude water features alongside a more clearly defined continuum level, indicative of a more isothermal atmosphere. The field-gravity L5 shows water feature amplitudes roughly 4 times stronger than the  $\gamma$  equivalent. Furthermore, with decreasing gravity, the height of the 2.2  $\mu m$  flux

peak grows by tens of percent relative to the 1.6  $\mu m$  peak.

The low-metallicity sequence for subtypes L0 and L7 is shown in Fig. 4. Decreasing metallicity at a fixed subtype imparts a drastic change in the appearance of the NIR region, showing a reversal in the relative heights of the opacity windows at 1.3 and 2.2  $\mu m$ . For both subtypes, the flux ratios of these features range

from  $\sim 0.5$  for the field objects to  $\sim 2.5$  for the esd objects. This change is leveraged for spectral metallicity classification, and is attributed to the onset of H<sub>2</sub>-H<sub>2</sub> pressure-broadened collisionally-induced absorption opacity (CIA). Namely, as the metallicity and therefore opacity of the atmosphere declines, the photosphere moves deeper to higher pressures where the broad continuum H<sub>2</sub>-H<sub>2</sub> CIA feature becomes a dominant opacity source from 1.7-3  $\mu\text{m}$ .

#### 4. MODEL GRIDS

We compare the observed spectra to five separate state-of-the-art model grids (see Table 4), each of which emphasizes different aspects of the thermochemistry, and includes or omits clouds. The grids are mostly spaced by 100 K in  $T_{\text{eff}}$  and 0.5 in  $\log(g)$ , with other variables changing by grid. These models emerge from an enormous variety of subjectively chosen input assumptions that govern the coupled composition, thermodynamics, and radiative transfer of each atmosphere. The selected molecular and continuum opacity databases, equations of state, atomic abundances, chemical reaction rates, thermodynamic coefficients, optical constants, convective mixing length scales—and the computational schemes connecting them—vary greatly from model to model. As we show in Fig. 5, even grid models with the same input temperature, gravity, and metallicity show relative flux differences as high as 2 at some wavelengths due to their different handling of chemistry. The models differ the most in the thermochemistry-sensitive 3-5  $\mu\text{m}$  region covering the features of CO, CH<sub>4</sub>, and CO<sub>2</sub>. Given that they have more differences than similarities, each grid represents a valiant independent attempt at emulating the delightfully complex atmospheres of brown dwarfs. The aim of our comparison is not to rank their relative “quality” or “truthfulness” but rather to see which input assumptions and parameters correlate with poor agreements between observations and models.

Each grid reports its spectra in different units. We convert each model to the spectral flux density  $F_\lambda$  [ $\text{W m}^{-2} \text{m}^{-1}$ ], which is the luminosity per wavelength emerging from a square meter of the object’s photosphere. These flux densities are then rescaled by the scaling factor

$$F_\lambda^{\text{obs}} = \left(\frac{R_\star}{d}\right)^2 F_\lambda^{\text{surf}} \quad (1)$$

where  $R_\star$  is the radius, and  $d$  is the measured distance to the object. We finally bring the model units to the Jy units of the SPHEREx observations

$$F_\nu(\text{mJy}) = F_\lambda \frac{\lambda^2}{c} \times 10^{29} \quad (2)$$

where  $\lambda$  and  $c$  are the wavelength and speed of light, respectively.

The following subsections describe each model grid in broad terms. Table 4 summarizes their key attributes, including their treatment of clouds and chemistry, their temperature ranges, native resolving power  $R_\lambda$  in the SPHEREx bandpass, and the other parameter dimensions. For more detailed descriptions of each model, the reader is referred to the first reference of each subsection, and the references within.

##### 4.1. ATMO2020

ATMO2020 (M. W. Phillips et al. 2020) is a coupled atmosphere-interior evolution grid computed at Solar metallicity using the state-of-the-art ATMO 1D radiative-convective equilibrium code. The models span 200-3000 K in 50-100 K intervals, and  $\log(g)$  2.5-5.5 in steps of 0.5 dex. This grid includes non-equilibrium chemistry, and parametrizes the vertical diffusion coefficient with a power-law gravity dependence ( $k_{zz} \propto g^{-2}$ ) to impose a constant dynamical timescale for objects of different mass. In addition to including chemical equilibrium models where the timescale for chemical equilibration is infinitesimal, they compute strong and weak non-equilibrium chemistry models, corresponding to  $k_{zz} = 10^4$  and  $10^6 \text{ cm s}^{-2}$  at  $\log(g) = 4.5$ , respectively. These values were selected following the finding of S. K. Leggett et al. (2017) that this range of vertical mixing best matches the [4.5] –  $M'$  (Spitzer Ch. 2 minus  $M'$  band) colors of late T- and Y-dwarfs at the same fixed gravity. As seen in Figs. 7 and 8 of that work, none of the several plotted model grids successfully predict the color-magnitude behavior across the full LTY span, with systematic departures on the order of 1-2 magnitudes. The models are downloaded from the ERC Opendata server<sup>18</sup>.

##### 4.2. ATMO2020++

The ATMO2020++ model grid (S. K. Leggett & P. Tremblin 2024) targets late T and Y dwarfs (250-1200 K), and includes a disequilibrium chemistry scheme with a fixed vertical mixing diffusion coefficient of  $k_{zz} = 10^7 \text{ cm s}^{-2}$ . This grid also uniquely computes a diabatic thermal profile in place of the usual adiabatic assumption, to better account for the disruption of convection by the observed rapid rotation of real brown dwarfs. This results in a cooler lower atmosphere, and a warmer

<sup>18</sup> <https://noctis.erc-atmo.eu/sharing/zyU96xA6o>

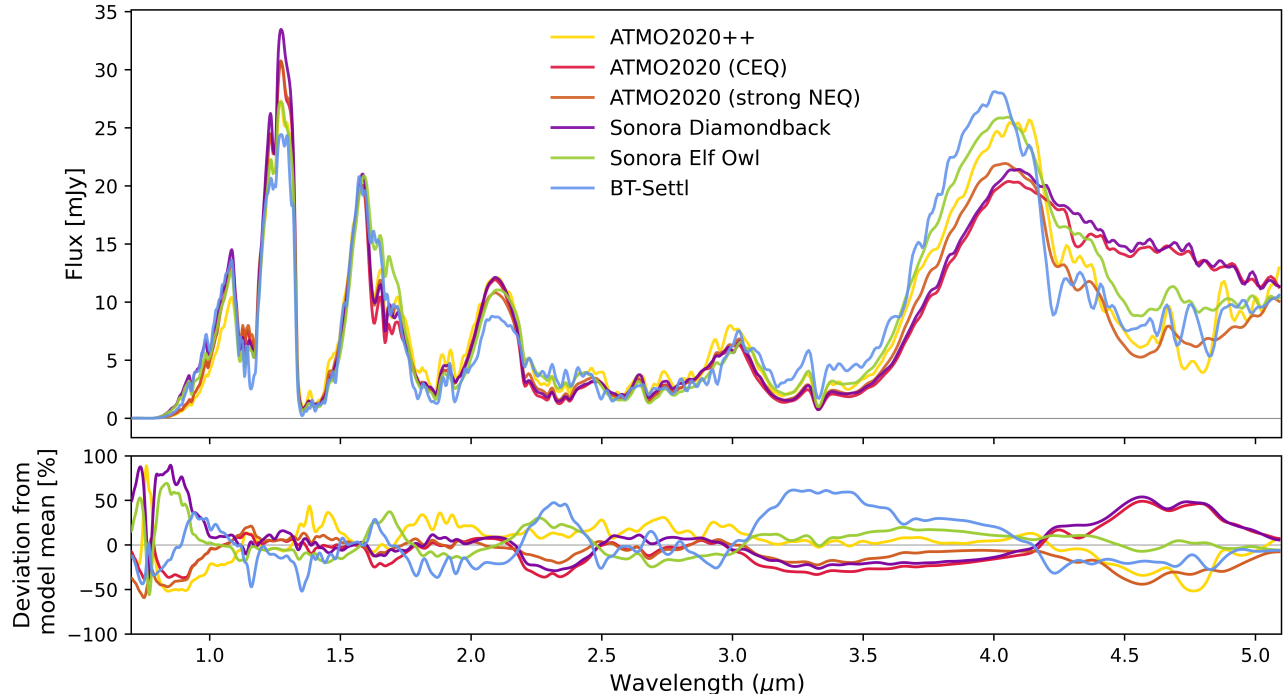


**Figure 5.** Top: Models of identical gravity ( $\log(g) = 5.5$ ), metallicity (Solar), and temperature (1200 K) for a  $1 R_J$  brown dwarf at 5 pc across all the grids considered in this work. Bottom: Each model’s percent residual relative to the smoothed mean of the models. The Elf Owl model has Solar C/O = 0.5, and  $\log(k_{zz}) = 2$  (weak mixing), and the Diamondback model is cloud-free with Solar C/O. Despite having identical temperature, gravity, and composition, the chemistry and mixing treatment have significant impacts on the spectra. The largest discrepancies (factor of  $\sim 2$ ) occur in the optical and the less-explored 3-5 micron region, where differing chemistry assumptions strongly influence the abundance ratios of the carbon species.

**Table 4.** Summary of model grids used in spectral fitting.

Grid	Cloud Treatment	Chemistry	$T_{\text{eff}}$ (K)	Varied Parameters	$R_\lambda$	$N$ models
ATMO2020++	Cloud-free	Non-eq.	200–1200	$T_{\text{eff}}, \log g, [\text{M}/\text{H}]$	3,000	299
ATMO2020	Cloud-free	Eq., non-eq.	200–3000	$T_{\text{eff}}, \log g, \text{chem. mode}$	1,000	510
BT-Settl	Microphysical (Rossow)	Eq.	400–2400	$T_{\text{eff}}, \log g$	8,000	106
Sonora: Elf Owl	Cloud-free	Non-eq.	275–2400	$T_{\text{eff}}, \log g, [\text{M}/\text{H}], \text{C}/\text{O}, k_{zz}$	60,000	43,252
Sonora: Diamondback	Sedimentation ( $f_{\text{sed}}$ )	Eq.	900–2400	$T_{\text{eff}}, \log g, [\text{M}/\text{H}], f_{\text{sed}}$	200,000	1,440

upper atmosphere. S. K. Leggett & P. Tremblin (2023) find that this grid better replicates the spectra of late-type brown dwarfs as measured by JWST. The grid is spaced by 25 K from 225 to 350 K, by 50 K from 350 to 450 K, and 100 K onward. The model log-gravity is spaced by 0.5 dex, and ranges from 2.5 to 5.5, which corresponds to a mass range of 0.12 to 120 Jupiter masses, assuming a Jupiter radius. The models are computed with metallicities of  $[\text{Fe}/\text{H}] = -0.5, 0.0, \text{ and } 0.3$ . We download the full grid from the ERC Opendata server<sup>19</sup>.

<sup>19</sup> <https://noctis.erc-atmo.eu/sharing/9puhIZma2>

### 4.3. BT Settl

The BT-Settl model grid is computed with the PHOENIX code, and includes a sophisticated parameter-free treatment of cloud formation and settling with vertical mixing (F. Allard et al. 2012, 2013; F. Allard 2014). The radiative-convective equilibrium model self-consistently computes the condensation of 55 optically active condensable species that contribute to a vertical grain size distribution profile informed by separate timescales for nucleation, condensation, and settling. These timescales are derived from more sophisticated 3D hydrodynamics (B. Freytag et al. 2010) and cloud microphysics (W. B. Rossow 1978) models. BT-Settl uses the now-outdated water opacities of R. J.

Barber et al. (2006). Despite this, the grid closely reproduces the  $J - K_s$  colors of stars, and also matches the bottom of the Main Sequence as it connects to the L dwarfs. We download the AGSS2009 400-2400 K,  $\log(g)$  3-5.5 Solar metallicity models from the SVO Theory Server<sup>20</sup>.

#### 4.4. Sonora Diamondback

The Sonora Diamondback coupled atmosphere-interior evolution grid (C. V. Morley et al. 2024) includes clouds parameterized using the mass-balance approach of (A. S. Ackerman & M. S. Marley 2001). The radiative-convective equilibrium models are computed using the approach of D. Saumon & M. S. Marley (2008) (and references therein). The parameter  $f_{\text{sed}}$  is held constant with height and encodes the cloud sedimentation efficiency, with small values resulting in thick clouds. The models incorporate the Mie scattering absorption coefficients of the amorphous form of 4 cloud species:  $\text{MgSiO}_3$ ,  $\text{Mg}_2\text{SiO}_4$ , Fe, and  $\text{Al}_2\text{O}_3$ . These are identified as the main contributors of aerosol opacity. The gradual contraction and cooling of the model interior is coupled to the thermal structure of the atmosphere: when a model atmosphere cools below  $\sim 1300$  K, the clouds suddenly clear, resulting in a brief stalling of the brown dwarf’s cooling and a brief acceleration in its contraction (e.g. Fig. 14 and 15, C. V. Morley et al. 2024). This theoretical prediction is seen as a local occurrence rate maximum in the observed population of brown dwarfs at the L/T transition (e.g., Fig. 17 of J. D. Kirkpatrick et al. 2024); (e.g., Fig. 13 of D. Saumon & M. S. Marley 2008). Infrared spectroscopy across the transition with Spitzer shows a similar clearing of the clouds, with  $f_{\text{sed}}$  rapidly rising below 1300 K and with fits preferring cloud-free models (e.g. D. C. Stephens et al. 2009). The Diamondback grid also includes cloud-free models, which show a lack of the distinctive evolutionary radius “bump.” While the models impose chemical equilibrium, they include the effect of vertical mixing via the vertical eddy diffusion coefficient  $k_{zz}$  varies with height and is computed using mixing length theory, without including  $k_{zz}$  as a free parameter (like Elf Owl). The Diamondback grid ranges from 900 to 2400 K, 3.5-5.5 in  $\log(g)$ , with  $f_{\text{sed}}$  spanning 1-8, and is computed at Solar, +0.5, and -0.5 metallicity. We download Version 2 of the full grid from Zenodo<sup>21</sup>.

#### 4.5. Sonora Elf Owl

The Sonora Elf Owl model grid (S. Mukherjee et al. 2024) is built using the same opacity database and a similar modeling approach to the Diamondback grid, but with an updated python-based implementation (S. Mukherjee et al. 2023). Unlike Diamondback, Elf Owl includes non-equilibrium chemistry due to vertical mixing, as governed by the fixed vertical mixing coefficient  $k_{zz}$ . Also unlike Diamondback, these atmosphere models are strictly cloud-free, and do not couple to an interior evolution scheme. The grid spans a wider range of temperatures than Diamondback, 275-2400 K, with a fine, 25 K spacing at the cold end. The strength of non-equilibrium chemistry governs the relative strengths of the carbon-bearing species in the mid-IR, with the  $\text{CO}/\text{CH}_4$  and  $\text{CO}_2/\text{CH}_4$  ratios varying by two orders of magnitude across the span of considered  $\log(k_{zz})$  values (2-9) for a 700 K object. The resulting effect is a factor of 2 flux difference in the carbon-rich 4.1-4.9  $\mu\text{m}$  region. The spread in metallicity has a similarly pronounced effect on the spectra in the same  $\text{CO}/\text{CO}_2$  region, and shows a strong influence on the flux window at 2.2  $\mu\text{m}$ , corresponding to the broadband continuum opacity of  $\text{H}_2\text{-H}_2$  collisional absorption. The relative strengths of the carbon features are not only sensitive to the vertical mixing and metallicity of the atmosphere, but also the carbon-to-oxygen ratio, which spans values of 0.5 (sub-Solar) to 2.5 (greatly enhanced) in the grid. The Elf Owl grid therefore represents an important early foray into disentangling the competing effects of non-equilibrium chemistry and composition. Future Sonora grids will additionally include clouds alongside non-equilibrium chemistry. We download the latest version of the full grid from Zenodo<sup>22</sup>.

## 5. SPECTRAL FITTING

We compare each measured spectrum to the ensemble of models, binning the models to the SPHEREx wavelength channels. We bin the models by taking the mean of the model flux values bounded by the bandwidth of each spectral measurement. Given the proximity of these objects, we neglect extinction by the interstellar medium. The stellar radius is fitted as a free parameter, while the distance is fixed to the central value of the distance measurement (see Eq. 1). The distance uncertainty is propagated through the radius uncertainty. The SPHEREx science team has examined repeat measurements of stable calibrators in the deep fields at the same wavelengths, which suggest a typical visit-to-visit

<sup>20</sup> [svo2.cab.inta-csic.es/theory/newov2/index.php?models=bt-settl-agss](https://svo2.cab.inta-csic.es/theory/newov2/index.php?models=bt-settl-agss)

<sup>21</sup> <https://zenodo.org/records/12735103>

<sup>22</sup> <https://zenodo.org/records/15150881>

RMS scatter of 3% (SPHERE Science Team, private comm.). This term will be added in later data processing, but we add it here in quadrature with the original flux uncertainties. In addition to estimating goodness-of-fit with  $\chi_\nu^2$ , we compute the  $G_k$  statistic as defined in Eq. 1 of M. C. Cushing et al. (2008), which weighs the information content of a spectral channel in proportion to its wavelength width. Given that the SPHEREx spectra vary from  $R \sim 40$  in the NIR to  $R \sim 110$  in the mid-IR, the  $G_k$  statistic prevents the narrower and lower-S/N channels from dominating the fits. We do not include the number of fitted grid variables in our goodness-of-fit estimates, since the goal is not to compare the different grids. Also, since the number of fitted points is in the hundreds to thousands, the effect of adding a couple of free parameters to the denominator is negligible.

The coarse nature of model grids makes for jagged, discretized fit posteriors which do not approximate a normal distribution. In this work, we intentionally restrict our model fits to the original parameter grid points rather than generating continuous posteriors through interpolation in  $T_{\text{eff}}$ ,  $\log(g)$ ,  $[\text{Fe}/\text{H}]$ , or cloud and chemistry parameters, as is common in the field. As a result, we do not quote formal uncertainties on the best-fitting parameters. The grids are coarsely sampled, with typical spacings of  $\Delta T_{\text{eff}} \sim 100$  K,  $\Delta \log(g) \sim 0.5$  dex, and  $\Delta [\text{Fe}/\text{H}] \sim 0.25 - 0.5$  dex. In practice, brown dwarf spectra can vary nonlinearly over comparable scales, especially near the L/T transition where cloud properties, vertical mixing, and chemistry change rapidly. Even sophisticated Bayesian fitting frameworks that account for interpolation uncertainties and correlated model residuals struggle to reconcile the temperatures, radii, metallicities, and gravities of well-studied benchmark objects, often finding systematic differences that are larger than the grid spacings (e.g., Z. Zhang et al. 2021). Using their interpolated Bayesian grid fitting approach, they find offsets on the order of 1.3 dex in  $\log(g)$  and 0.4 dex in  $[\text{Fe}/\text{H}]$  for well-understood benchmark objects, which is much larger than the spacing of their grids. With their “traditional” interpolated grid-fitting approach, they report similar offsets, with uncertainties that are questionably 10 or even 100 times smaller than the grid spacing. Alternatively, sophisticated atmospheric retrievals with flexible atmospheric profiles (e.g., M. R. Line et al. 2017; J. D. Lothringer et al. 2024) produce true posteriors and covariances, but are beyond the scope of the present work. Therefore, to avoid constructing posteriors with assumptions of the subgrid behavior, and to avoid imposing additional and unjustified systematics, we elect to instead report the best-fitting 10% of native models for each grid, and leave a more sophisticated model fit-

ting analysis for a future study. These best-fitting model parameters along with their goodness-of-fit are included in a machine-readable table, which one may interpolate if they wish to derive sub-grid best-fit parameters and confidence intervals.

A handful of selected spectral fits are shown below, in Figures 6, 7, 8, 10, 11, and 12. The figure legends report the temperature,  $\chi_\nu^2$ , radius scaling, metallicity, and gravity for each best-fit model. For the Diamondback and Elf Owl models, the legends also report the model’s  $f_{\text{sed}}$  and  $\log(k_{\text{zz}})$ , respectively.

The color image in each figure’s inset is a median shift-aligned and distortion-corrected stack  $2.5' \times 2.5'$  of all available SPHEREx images centered on the target. The blue color channel is assigned to the median of Bands 1 and 2, green assigned to the median of Bands 3 and 4, and red assigned to the median of Bands 5 and 6. The images are aligned to the celestial coordinate grid, with North pointing up and East pointing left.

None of the model grids stand out with exceptional fit quality, with  $\chi_\nu^2 \geq 10$  for the majority of spectra with high S/N. In this regime, the best-fit model parameters do not necessarily reflect the true properties of the object. In the next section, we attempt a different approach at comparing the behavior of the models to the observed sequence.

### 5.1. Model Intercomparison

Population studies of brown dwarfs and exoplanets using the 2MASS/WISE filters, and post-cryo Spitzer/IRAC observations have been conducted (e.g., B. M. Patten et al. 2006; C. Baxter et al. 2021; A. Sanghi et al. 2023), but these broadband filters do not have the resolution or placement to identify individual chemical features, and therefore fail to distill the chemistry information. To leverage the wavelength and spectral type coverage of SPHEREx, and to better identify specific model deficiencies, we define a set of custom spectral indices corresponding to the thermochemically sensitive carbon species in the 3-5  $\mu\text{m}$  range. We define three wavelength ranges centered on the most prominent absorption features of  $\text{CH}_4$ ,  $\text{CO}_2$ , and  $\text{CO}$ , and compute their magnitudes normalized relative to the universally prominent 4  $\mu\text{m}$  opacity window, which lands between fundamental water absorption bands and encapsulates a region of declining  $\text{CH}_4$  opacity. The magnitude of a given index species  $M_i$  is given by

$$M_i = -2.5 \log_{10} \left( \frac{F_i}{F_{\text{norm}}} \right) \quad (3)$$

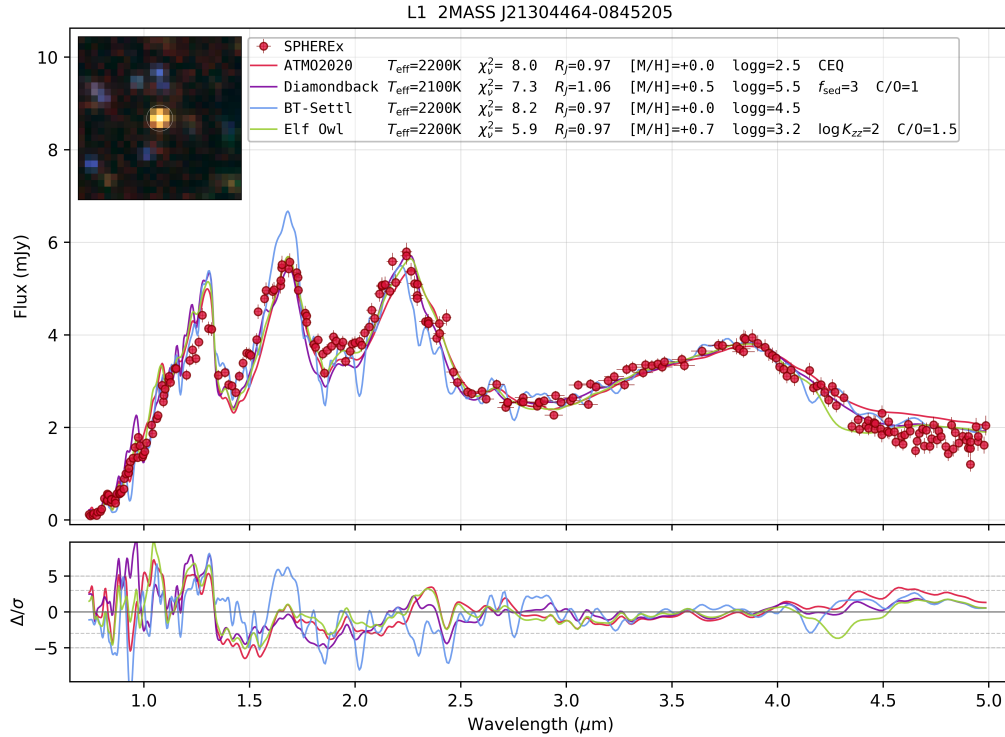


**Figure 6.** The L1 spectral standard dwarf 2MASS J21304464-0845205. The inset RGB image is the median-stacked SPHEREx image data (see text for full description). The bottom panel shows the flux residuals of the models from the smoothed and interpolated data. The best-fitting models span 100 K in effective temperature, contributing to a  $\sim 10\%$  systematic range in the best-fit radius. The cloudy Diamondback and BT-Settl models best capture the amplitudes of the NIR opacity windows and the mid-IR water absorption. All models have  $\chi^2_{\nu} \geq 5$ , and span 3 orders-of-magnitude in best-fit gravity.

where  $F_i$  is the mean of the in-band flux, and  $F_{\text{norm}}$  is the mean of the reference or normalization region. The magnitude uncertainties  $\sigma_I$  are given by

$$\sigma_M = \frac{2.5}{\ln 10} \left[ \left( \frac{\sigma_F}{F} \right)^2 + \left( \frac{\sigma_{F_{\text{norm}}}}{F_{\text{norm}}} \right)^2 \right]^{1/2} \quad (4)$$

where  $\sigma_F$  and  $\sigma_{F_{\text{norm}}}$  are the quadrature-summed flux uncertainties within the respective bands. We select the spectral indices visually, using the high-S/N spectrum of the T6 DENIS J081730.0-615520, and the opacity ranges in Fig. 1 to place the region boundaries (see Table 5 and Fig. 13). We find that using narrower ranges does not necessarily improve the color contrast or the strengths of the trends, but does hurt the SNR of the measurements. These regions are somewhat contaminated by overlapping molecules, making them imperfect chemical indicators. Indeed, the lack of a clean continuum baseline flux level in any wavelength region makes brown dwarf spectra a challenge to interpret.

We next compute the same chemical indices for each model grid as a function of temperature, at a fixed  $\log(g)$  of 5, and compare the grids to the models in Figures 14 and 15, showing CO and CO<sub>2</sub> as a function of CH<sub>4</sub> strength, respectively. Higher values of the

**Table 5.** Wavelength ranges of our spectral indices.

Index	Feature region ( $\mu\text{m}$ )	Norm. region ( $\mu\text{m}$ )
CH <sub>4</sub>	3.20–3.65	3.70–4.14
CO <sub>2</sub>	4.18–4.35	3.70–4.14
CO	4.55–4.80	3.70–4.14

indices generally correspond to stronger absorption by that molecule, and this is made apparent by the trend of increasing CH<sub>4</sub> index with later spectral subtypes. Each spectral subtype is labeled, and the grid model temperatures are sparsely labeled to minimize visual crowding. The Y-dwarfs are excluded from these figures due to their low SNR in the CH<sub>4</sub> band, which is undetected by SPHEREx.

The sequence of observed field brown dwarfs shows fairly continuous and smooth behavior, with the spectral types increasing nearly monotonically from left to right. The Elf Owl models are shown with weak and strong vertical mixing (dashed and solid green lines, respectively), and the Diamondback models are similarly shown with and without clouds (solid and dashed purple

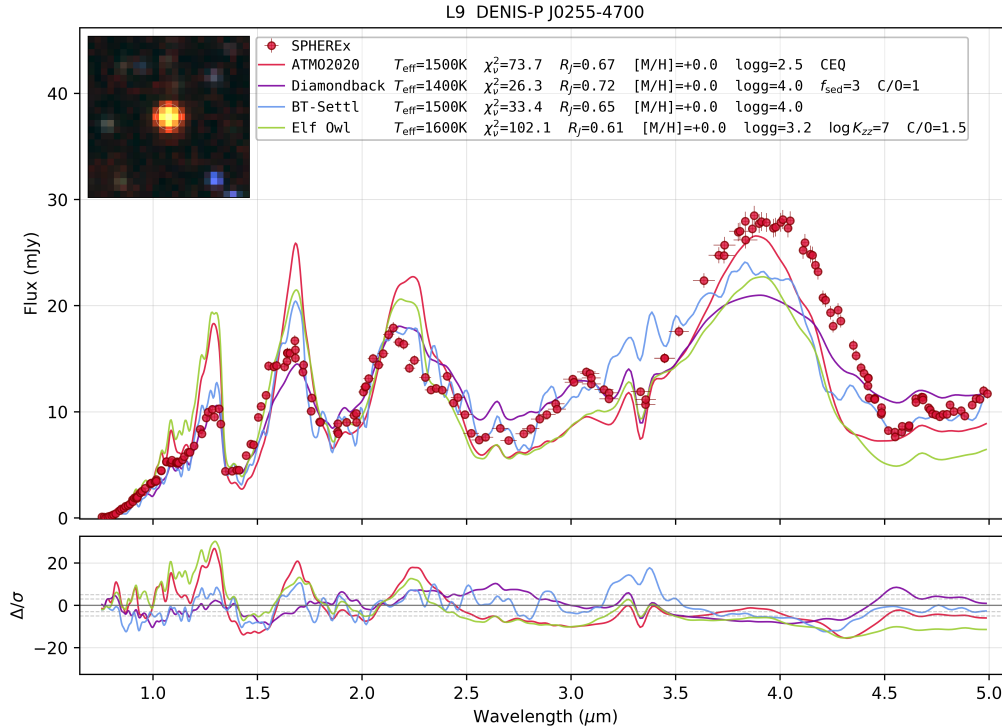


**Figure 7.** Same as Fig. 6, but for the L9 spectral standard dwarf DENIS J025503.3-470049. The Sonora Diamondback fit prefers a cloudy model, and the Elf Owl fit indicates a preference for strong non-equilibrium chemistry, but with  $\chi^2_{\nu} \geq 20$ , these conclusions are not well supported by the data. The 200-K span in recovered temperature, and the unphysically small and disparate radii, further illustrate the negative impact of model systematics on the trustworthiness of recovered physical parameters. The Diamondback model prefers clouds, which help reduce the prominence of the J, H and 4  $\mu\text{m}$  peaks, helping the fit quality on the blue end of the spectrum.

lines, respectively). Two chemistry variants of ATMO 2020, chemical equilibrium and strong non-equilibrium, are shown as light and dark orange lines, respectively.

## 6. DISCUSSION

While no grid matches spectra across the sequence, all of them qualitatively capture the general trend of CO and CO<sub>2</sub> with CH<sub>4</sub> abundance, showing a gradual rise from subtype L0 through T3 ( $\sim 2300$ -1200 K), and then rapidly descending by 1.5 magnitudes for the cooler, CH<sub>4</sub>-dominated objects (Fig. 14, Fig. 15). The CO<sub>2</sub> index trend is similar in shape, with a maximum at subtype T5 ( $\sim 1000$  K), though the models tend to under-predict the strength of the CO<sub>2</sub> feature for the L dwarfs (Fig. 15). The Elf Owl models with weaker vertical mixing ( $\log k_{zz} = 4$ ) much more closely match the observations than the models with stronger mixing ( $\log k_{zz} = 8$ ). The same is seen for the ATMO2020 models, with the data aligning more with the stronger non-equilibrium chemistry model line. The T dwarfs show a CO dropoff of a similar magnitude to the Elf Owl low  $k_{zz}$  and ATMO2020 strong non-equilibrium (NEQ) models, while the earlier T and L dwarfs veer more toward the equilibrium models. The addition of clouds to

the Diamondback models results in worse agreement in the CO index, and none of the models are able to match the strength of the CH<sub>4</sub> feature for objects later than T7. The CO magnitudes of the mid-T dwarfs appear well-represented by the Elf Owl (low  $k_{zz}$ ), ATMO2020 (weak NEQ), BT-Settl, and ATMO2020++ model grids alike, and this is corroborated by the relatively good fit statistics for these objects.

The observed CO/CH<sub>4</sub> sequence appears to qualitatively lie along a smooth, curved trend line, with deviations on the order of 0.2 mag. The relatively monotonic progression of spectral type with CH<sub>4</sub> index, and the fairly regular spacing along this axis, indicates that CH<sub>4</sub> opacity varies smoothly with temperature, or more tautologically that it dominates the spectral classification. The lack of stochasticity may be an indication that either our sample size is too small or well-curated to see much astrophysical scatter, or that the chemical trends are relatively robust against individuality, following a well-traveled path in chemistry/cooling space. More objects with well-defined spectral subtypes are needed to comment on this empirical observation. The recent works of J. Gagné et al. (2026), H. Brooks et al. (2026), and Z. Tu et al. (2026) present other sequences

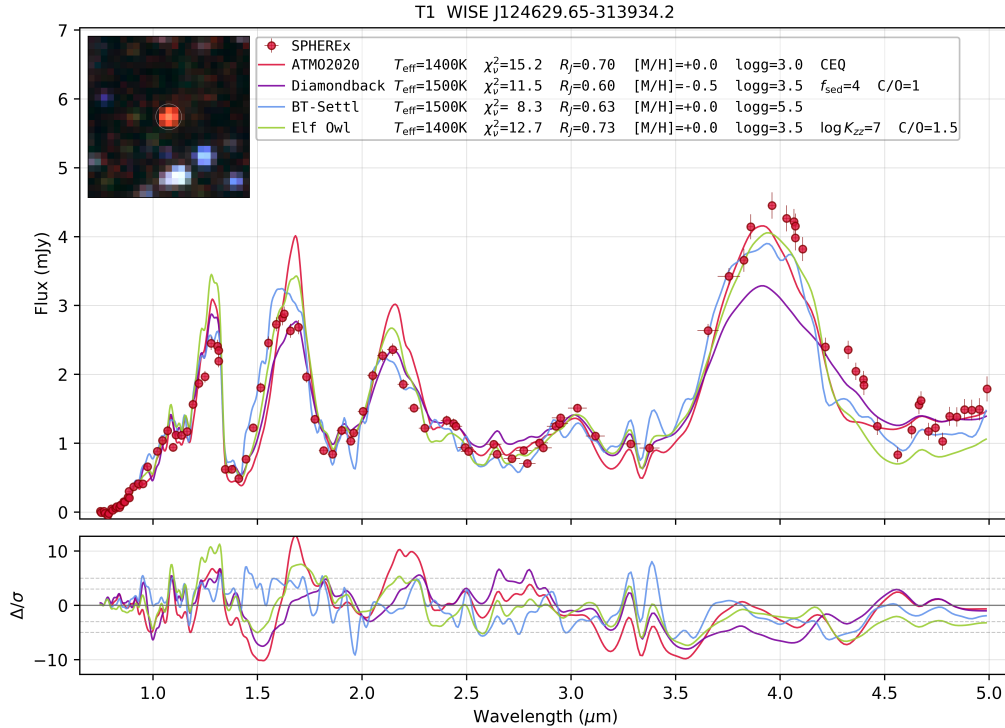


**Figure 8.** Same as Fig. 7, but for the T1 dwarf WISE J124629.65-313934.2. All models fail to capture the true amplitude of the  $4 \mu\text{m}$  opacity window, while most models overestimate the J/H/K peaks. All models find radii that are considerably smaller than theoretical expectations, with a systematic scatter of  $\sim 20\%$  partially resulting from the 100 K range in effective temperature. The best-fit models are  $\sim 200$  K warmer than expected for a typical T1 dwarf, possibly due to overfitting of the  $4 \mu\text{m}$  peak.

of SPHEREEx brown dwarf spectra. The studies of H. Brooks et al. (2026) and J. Gagné et al. (2026) show similar broad  $\text{H}_2\text{O}$ , CO,  $\text{CO}_2$ , and  $\text{CH}_4$  morphology across ultracool spectral types, and the sample of Z. Tu et al. (2026) also quantitatively recovers smooth molecular-index trends and a CO/ $\text{CO}_2$  turnover near  $\sim 1000$  K.

Lastly, the wide range of parameter space explored by Elf Owl gives a unique opportunity to test their observability and crosstalk. In Fig. 16 of the Appendix, we show the  $\text{CH}_4$  index against CO– $\text{CO}_2$  for one-parameter slices through the Elf Owl grid to test the coupling of the carbon chemistry in the grid. CO– $\text{CO}_2$  captures the relative behavior of the two carbon-oxygen species, which are chemically linked to  $\text{CH}_4$  through the temperature-, metallicity-, and mixing-dependent partitioning of carbon among CO,  $\text{CO}_2$ , and  $\text{CH}_4$  (e.g., J. J. Fortney et al. 2020; D. K. Sing et al. 2024). The figure shows the same spectral sequence across varying vertical mixing, gravity, metallicity, and C/O ratio. Changing the vertical mixing and metallicity parameters results in the most CO– $\text{CO}_2$  variance at a fixed  $\text{CH}_4$  index. Namely, increasing the vertical mixing from weak ( $\log(k_{zz}) = 2$ ) to Jupiter-like ( $\log(k_{zz}) = 7$ ) at Solar metallicity results in 0-, 0.5-, and 1-dex differences in CO– $\text{CO}_2$  for L’s,

mid-T’s and late-T’s, respectively. A population-wide study of T dwarf carbon chemistry shows that they have  $\log(k_{zz}) = 5 - 8$ , which is higher than the  $\log(k_{zz}) = 2-4$  values inferred from the plot. At Solar metallicity, the CO– $\text{CO}_2$  remains roughly constant, with just 0.5-dex of variation across the sequence. However, at a wider range of modeled [M/H] values, the models overlap at constant  $\text{CH}_4$  index, making the CO– $\text{CO}_2$  index degenerate in the interpretation of atmospheric metallicity. C/O ratio and  $\log(g)$  contribute a further 0.5-dex of scatter, each. The fact that none of the Elf Owl cross-cuts seem to reproduce the sequence suggests that either our sample of objects spans a gradient in composition and thermochemistry, or that the imperfect spectral fits are due to some inherent model deficiency causing the indices to be poor representations of the chemical trends. Above all, the Fig. 16 shows that the chemistry-sensitive carbon species map a complex and degenerate space, and that future population-level inferences will require other thermochemical signatures, such as the NIR water features, to break these degeneracies.

## 7. CONCLUSION

In this work, we have presented 37 SPHEREEx spectra of the nearest and highest-S/N L0-Y4 brown dwarfs

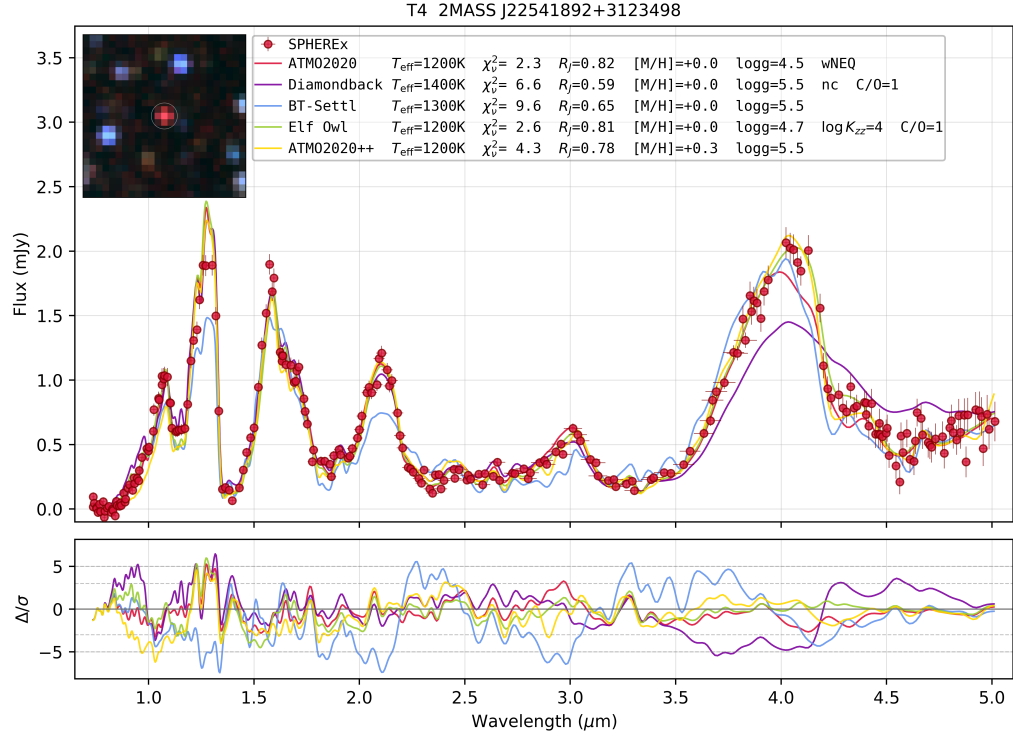


Figure 9. Same as Fig. 7, but for the T4 dwarf 2MASS J22541892+3123498.

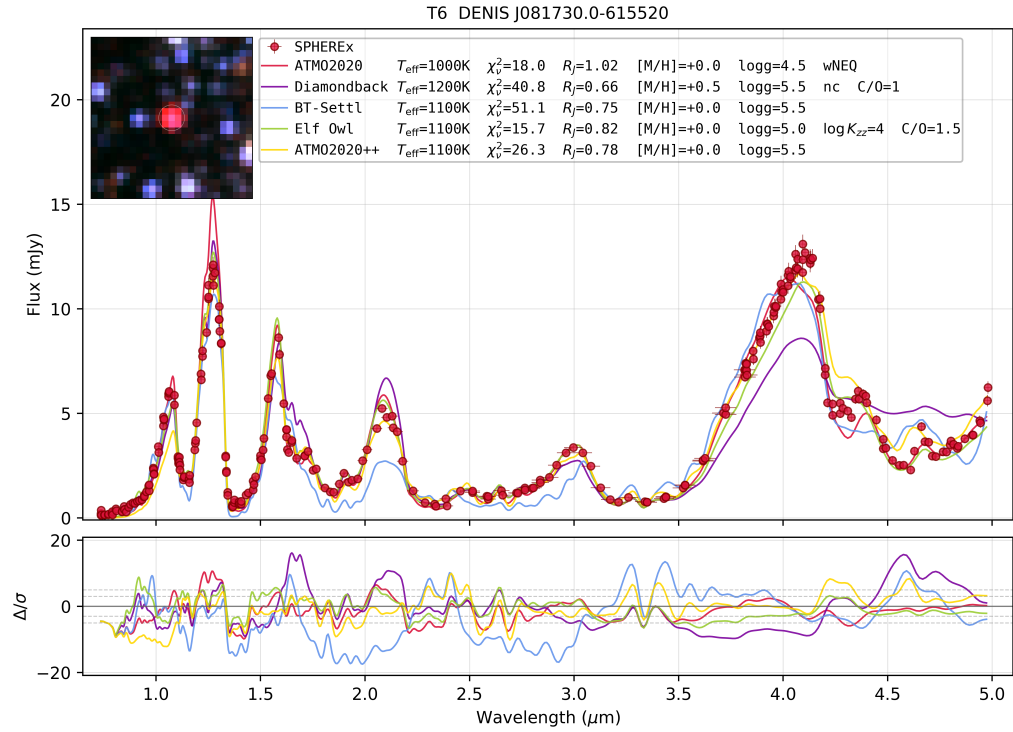
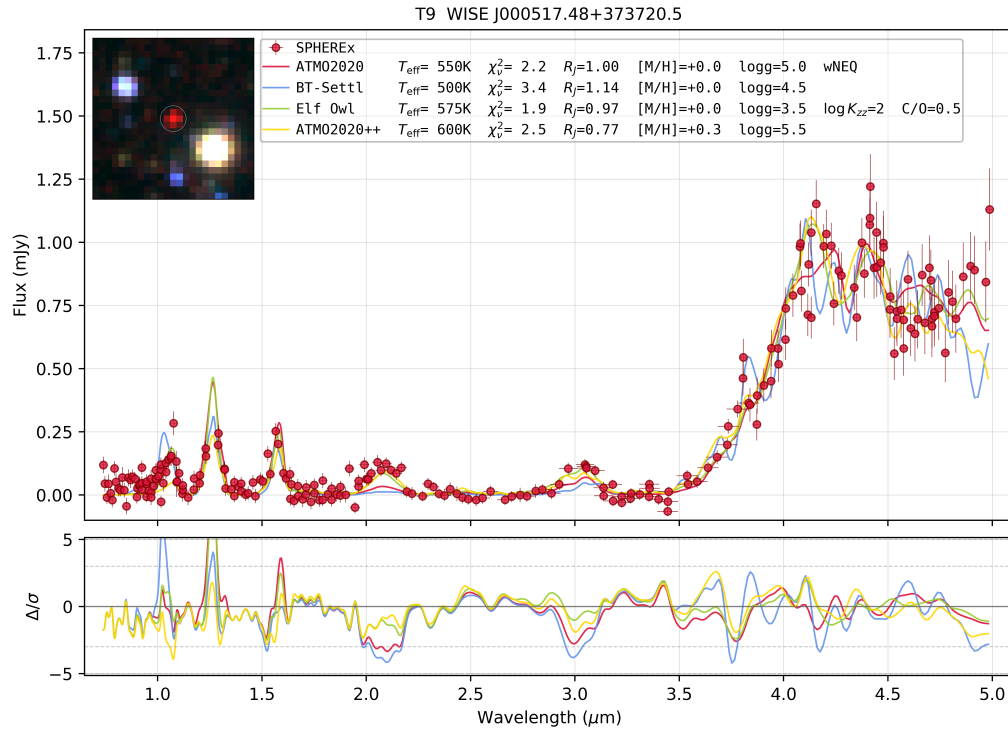
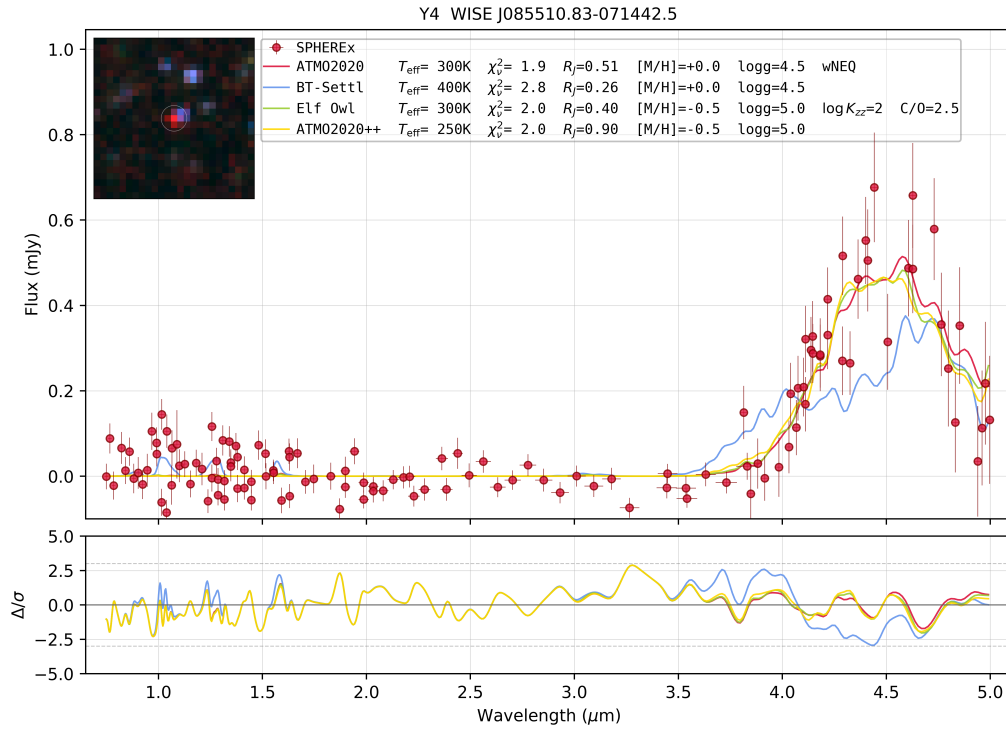


Figure 10. Same as Fig. 7, but for the T6 dwarf DENIS J081730.0-615520. The strong absorption seen at the red end of the spectrum indicate a relatively high abundance of CO and CO<sub>2</sub>.



**Figure 11.** Same as Fig. 7, but for the T9 dwarf WISE J000517.48+373720.5. The best-fitting models range from 550-650 K, and yield radii that systematically differ by  $\sim 50\%$ . The recovered metallicities similarly vary strongly between the models, ranging from strongly sub-Solar to super-Solar. Unlike the hotter T6 dwarf, this T9 shows relatively weak CO and CO<sub>2</sub> absorption.



**Figure 12.** Same as Fig. 7, but for the  $\gtrsim$ Y4 dwarf WISE J085510.83-071442.5, the coldest brown dwarf known. Only flux redward of  $3.9 \mu\text{m}$  is detected reliably. The factor of 3-4 span of recovered radii demonstrates the enormous systematic uncertainties associated with the characterization of Y dwarfs with atmosphere models.

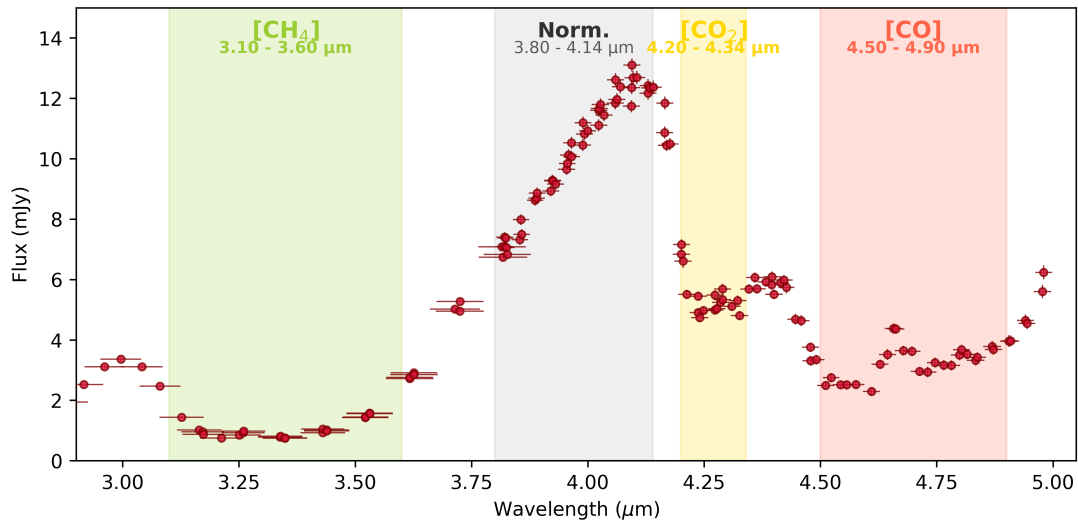


**Figure 13.** A schematic showing the ranges of the spectral indices defined in this work overlaid with the representative spectrum of the T6 dwarf DENIS J081730.0-615520. The  $4 \mu\text{m}$  opacity window is the closest any spectrum gets to the “continuum” flux level, and it stands out across the full sequence of brown dwarfs, making it a natural anchor point.

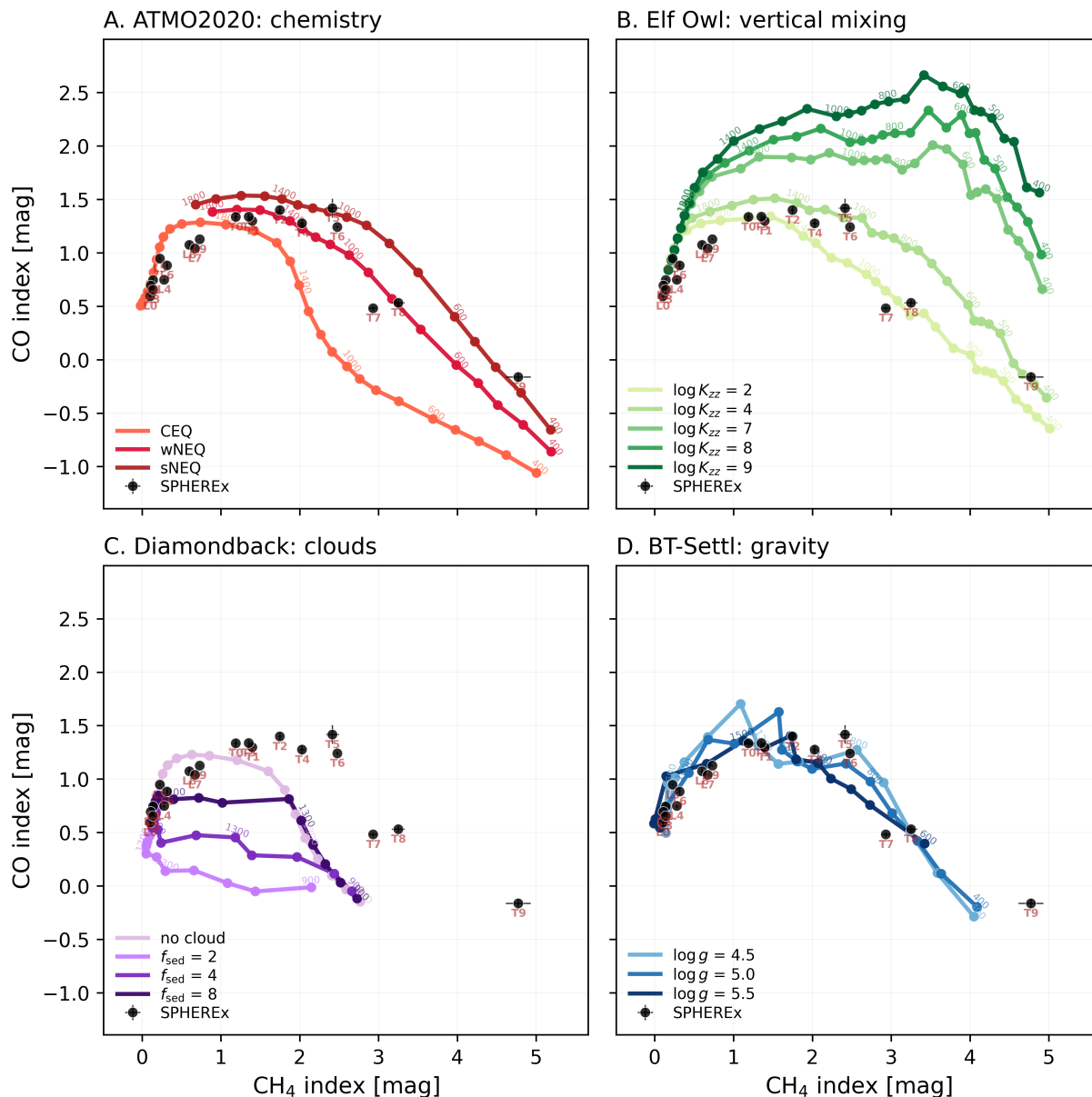


**Figure 14.** The relative strengths of the CH<sub>4</sub> and CO magnitude indices for the SPHEREx field brown dwarf sequence (black points) (Table 1) compared to four model grids. The models all share Solar metallicity ( $[Fe/H] = 0$ ) and C/O ratio, and have  $\log(g) = 5$ , except for BT-Settl, which spans a range of  $\log(g)$ . Stronger CH<sub>4</sub> and CO absorption results in a larger index value and corresponds to higher abundances of those gases. The CO index drops precipitously from type T6 to type T7, spanning  $\sim 1000$  to  $700$  K. Meanwhile, the CH<sub>4</sub> index varies smoothly across this chemical transition.

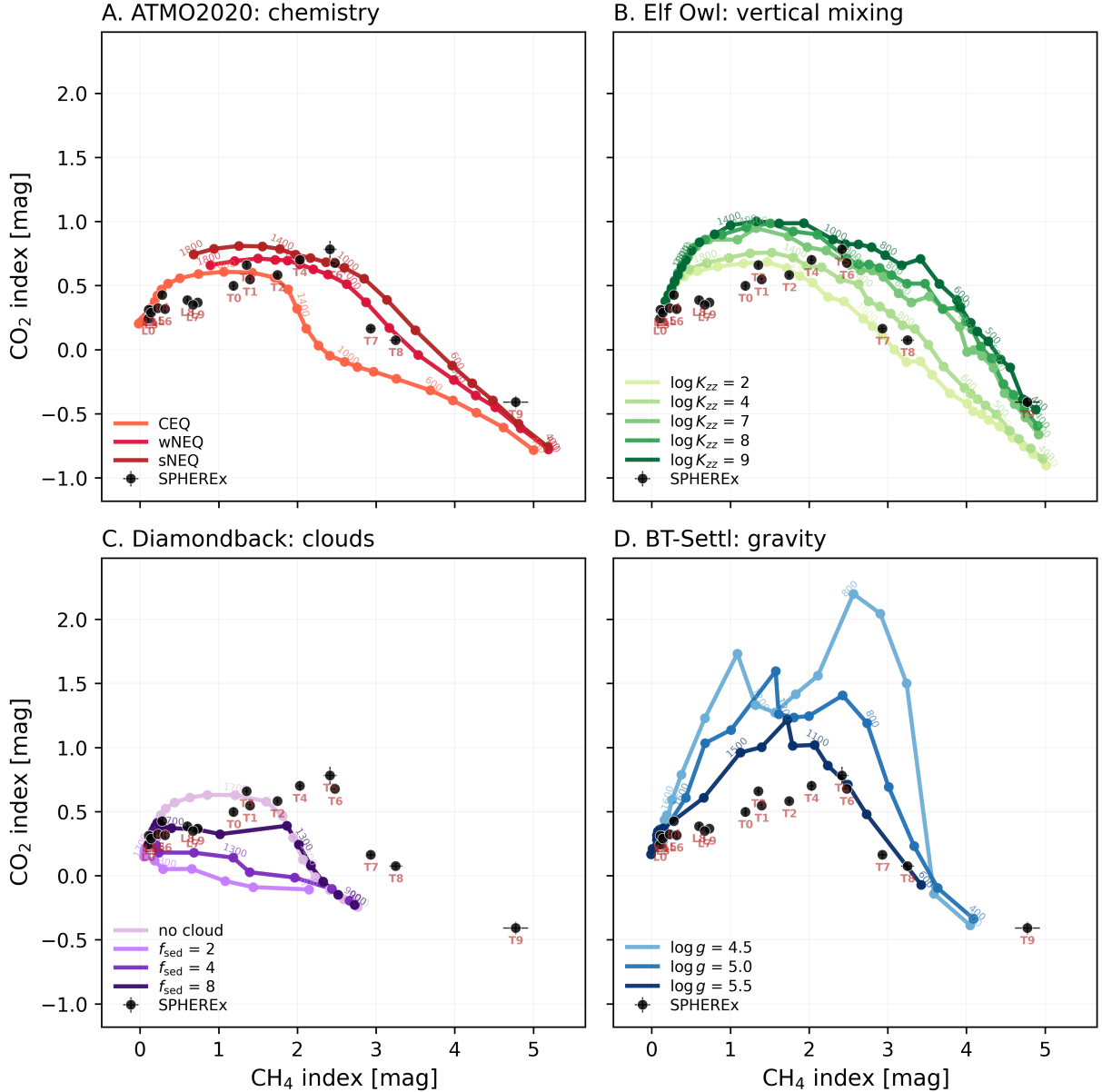


**Figure 15.** The relative strengths of the CH<sub>4</sub> and CO<sub>2</sub> magnitude indices for the SPHEREx field brown dwarf sequence (black points) (Table 1) compared to models. The models all share Solar metallicity ( $[\text{Fe}/\text{H}] = 0$ ) and C/O ratio, and have  $\log(g) = 5$ , except for BT-Settl, which spans a range of  $\log(g)$ . Stronger CH<sub>4</sub> and CO<sub>2</sub> absorption results in a larger index value and corresponds to higher abundances of those gases. Similarly to the CO index, the CO<sub>2</sub> index decays significantly from spectral type T6 to T7, indicative of a chemical transition between  $\sim 1000$  and 700 K.

spanning the full range of spectral subtypes (Fig. 2). As SPHEREx continues mapping the sky, these spectra will grow in S/N with the growing spectral sampling density, enabling more detailed investigations of their chemistry and variability. However, even the first-epoch SPHEREx spectra analyzed here reveal that state-of-the-art brown dwarf model grids generally fail to trace their complex features, meaning that our understanding of their nature is limited by model systematics rather than observational uncertainty. By examining

the sequence through the lens of the thermochemically active species, which are now readily accessible with SPHEREx, we show that the models generally approximate the smoothly coherent abundance trends of CO and CO<sub>2</sub> as they are converted to CH<sub>4</sub> with declining temperature and increasing age. We also show that the addition of clouds does not improve Diamondback model fits (see Figs. 14 and 15), especially at the cloudy L/T transition (see Fig. 7), implying the need for more theoretical work connecting clouds with chemistry. Opti-

mistically, the models seem to qualitatively represent the low-gravity and low-metallicity L dwarfs (see Fig. 17, 18, 19, and 20, which probe a more extreme regime of parameter space. Future observational studies with expanded statistical samples will closely explore empirical trends with luminosity and age, while other works will attempt to decipher the competing effects of vertical mixing, metallicity, and bulk composition.

#### ACKNOWLEDGEMENTS

We thank Federico Marocco and Rocío Kiman for their fruitful discussions about spectral fitting. We additionally thank Jonathan Fortney and Caroline Morley for their suggestions on which models to use.

The SPHEREx spectral image data used in this work were obtained from the SPHEREx Quick Release Spectral Images, QR2 ( [SPHEREx Team 2025](#)), served by IRSA/IPAC. We acknowledge support from the SPHEREx project under a contract from the NASA/Goddard Space Flight Center to the California Institute of Technology. Part of the research described in this paper was carried out at the Jet Propulsion Laboratory, California Institute of Technology, under a contract with the National Aeronautics and Space Administration (80NM0018D0004). The authors acknowledge the Texas Advanced Computing Center (TACC) at The University of Texas at Austin for providing computational resources that have contributed to the research results reported within this paper.

#### APPENDIX

#### REFERENCES

- Ackerman, A. S., & Marley, M. S. 2001, *ApJ*, 556, 872, doi: [10.1086/321540](#)
- Akeson, R., Dubois-Felsmann, G. P., Crill, B. P., et al. 2025, arXiv e-prints, arXiv:2511.15823, doi: [10.48550/arXiv.2511.15823](#)
- Allard, F. 2014, in *IAU Symposium*, Vol. 299, Exploring the Formation and Evolution of Planetary Systems, ed. M. Booth, B. C. Matthews, & J. R. Graham, 271–272, doi: [10.1017/S1743921313008545](#)
- Allard, F., Homeier, D., & Freytag, B. 2012, *Philosophical Transactions of the Royal Society of London Series A*, 370, 2765, doi: [10.1098/rsta.2011.0269](#)
- Allard, F., Homeier, D., Freytag, B., Schaffenberger, W., & Rajpurohit, A. S. 2013, *Memorie della Societa Astronomica Italiana Supplementi*, 24, 128, doi: [10.48550/arXiv.1302.6559](#)
- Ashby, M., et al. 2026, in prep.
- Baraffe, I., Chabrier, G., Barman, T. S., Allard, F., & Hauschildt, P. H. 2003, *A&A*, 402, 701, doi: [10.1051/0004-6361:20030252](#)
- Barber, R. J., Tennyson, J., Harris, G. J., & Tolchenov, R. N. 2006, *MNRAS*, 368, 1087, doi: [10.1111/j.1365-2966.2006.10184.x](#)
- Batalha, N. E., Marley, M. S., Lewis, N. K., & Fortney, J. J. 2019, *ApJ*, 878, 70, doi: [10.3847/1538-4357/ab1b51](#)
- Baxter, C., Désert, J.-M., Tsai, S.-M., et al. 2021, *A&A*, 648, A127, doi: [10.1051/0004-6361/202039708](#)
- Beiler, S. A., Cushing, M. C., Kirkpatrick, J. D., et al. 2024, *ApJ*, 973, 107, doi: [10.3847/1538-4357/ad6301](#)
- Bock, J. J., Aboobaker, A. M., Adamo, J., et al. 2025, arXiv e-prints, arXiv:2511.02985, doi: [10.48550/arXiv.2511.02985](#)
- Boeshaar, P. C., & Tyson, J. A. 1985, *AJ*, 90, 817, doi: [10.1086/113791](#)
- Borysow, A. 2002, *A&A*, 390, 779, doi: [10.1051/0004-6361:20020555](#)
- Bradač, M., Willott, C., Asada, Y., et al. 2026, Two Exciting High-redshift Galaxy Candidates Turn Out to Be Two Exciting Ultra-cool Brown Dwarfs, <https://arxiv.org/abs/2604.23668>
- Brooks, H., Cushing, M. C., & Kothari, H. 2026, *Research Notes of the AAS*, 10, 94, doi: [10.3847/2515-5172/ae6257](#)
- Bryan, S., Bock, J., Burk, T., et al. 2025, <https://arxiv.org/abs/2508.20332>
- Burgasser, A. J., Geballe, T. R., Leggett, S. K., Kirkpatrick, J. D., & Golimowski, D. A. 2006, *ApJ*, 637, 1067, doi: [10.1086/498563](#)
- Burgasser, A. J., Gonzales, E. C., Beiler, S. A., et al. 2025, *Science*, 390, 697, doi: [10.1126/science.adu0401](#)
- Burrows, A., Hubbard, W. B., Lunine, J. I., & Liebert, J. 2001, *Reviews of Modern Physics*, 73, 719, doi: [10.1103/RevModPhys.73.719](#)
- Burrows, A., Marley, M., Hubbard, W. B., et al. 1997, *ApJ*, 491, 856, doi: [10.1086/305002](#)

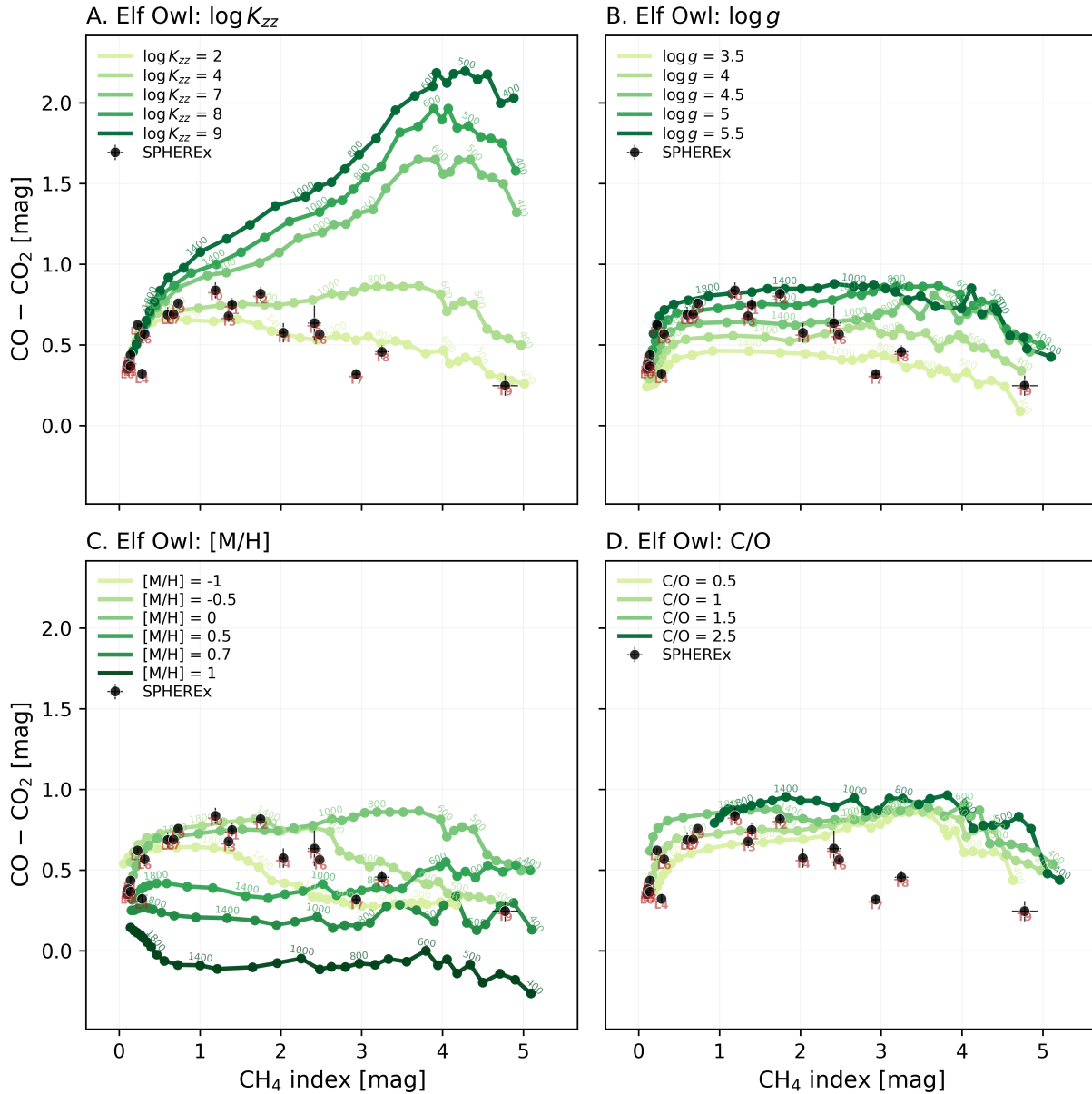


**Figure 16.** The relative strength of the CH<sub>4</sub> index versus the difference of the CO and CO<sub>2</sub> indices for the SPHEREx field brown dwarf sequence (black points) (Table 1) compared to the various Elf Owl free parameters. Unless otherwise indicated by the legend, the models have Solar metallicity and C/O ratio, with  $\log(g) = 5.0$ , and  $\log(k_{zz}) = 4.0$ .

Caselden, D., Westin, III, P., Meisner, A., Kuchner, M., & Colin, G. 2018, WiseView: Visualizing motion and variability of faint WISE sources., Astrophysics Source Code Library, record ascl:1806.004 <http://ascl.net/1806.004>

Cruz, K. L., Kirkpatrick, J. D., & Burgasser, A. J. 2009, *AJ*, 137, 3345, doi: [10.1088/0004-6256/137/2/3345](https://doi.org/10.1088/0004-6256/137/2/3345)

Cushing, M. C., Marley, M. S., Saumon, D., et al. 2008, *ApJ*, 678, 1372, doi: [10.1086/526489](https://doi.org/10.1086/526489)

Cushing, M. C., Kirkpatrick, J. D., Gelino, C. R., et al. 2011, *ApJ*, 743, 50, doi: [10.1088/0004-637X/743/1/50](https://doi.org/10.1088/0004-637X/743/1/50)

Dupuy, T. J., & Liu, M. C. 2017, *ApJS*, 231, 15, doi: [10.3847/1538-4365/aa5e4c](https://doi.org/10.3847/1538-4365/aa5e4c)

Faherty, J. K., Burningham, B., Gagné, J., et al. 2024, *Nature*, 628, 511, doi: [10.1038/s41586-024-07190-w](https://doi.org/10.1038/s41586-024-07190-w)

Filippazzo, J. C., Rice, E. L., Faherty, J., et al. 2015, *ApJ*, 810, 158, doi: [10.1088/0004-637X/810/2/158](https://doi.org/10.1088/0004-637X/810/2/158)

Fortney, J. J., Visscher, C., Marley, M. S., et al. 2020, *AJ*, 160, 288, doi: [10.3847/1538-3881/abc5bd](https://doi.org/10.3847/1538-3881/abc5bd)

Freytag, B., Allard, F., Ludwig, H.-G., Homeier, D., & Steffen, M. 2010, *A&A*, 513, A19, doi: [10.1051/0004-6361/200913354](https://doi.org/10.1051/0004-6361/200913354)

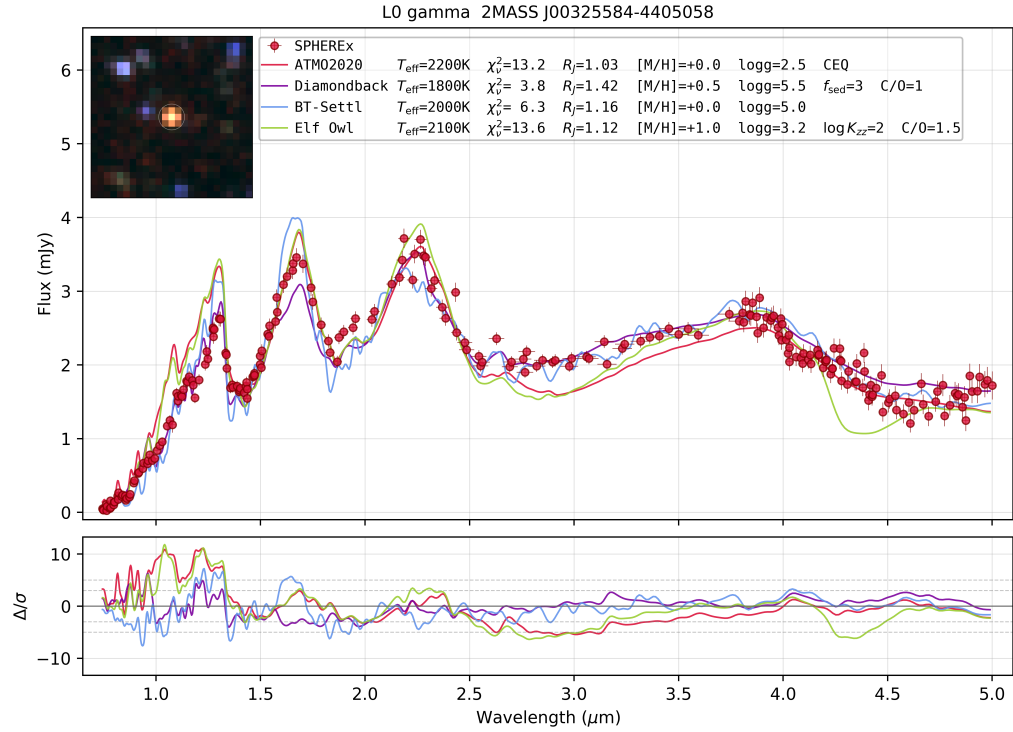


**Figure 17.** Same as Fig. 7, but for the low-gravity L0 $\gamma$  dwarf 2MASS J00325584-4405058.

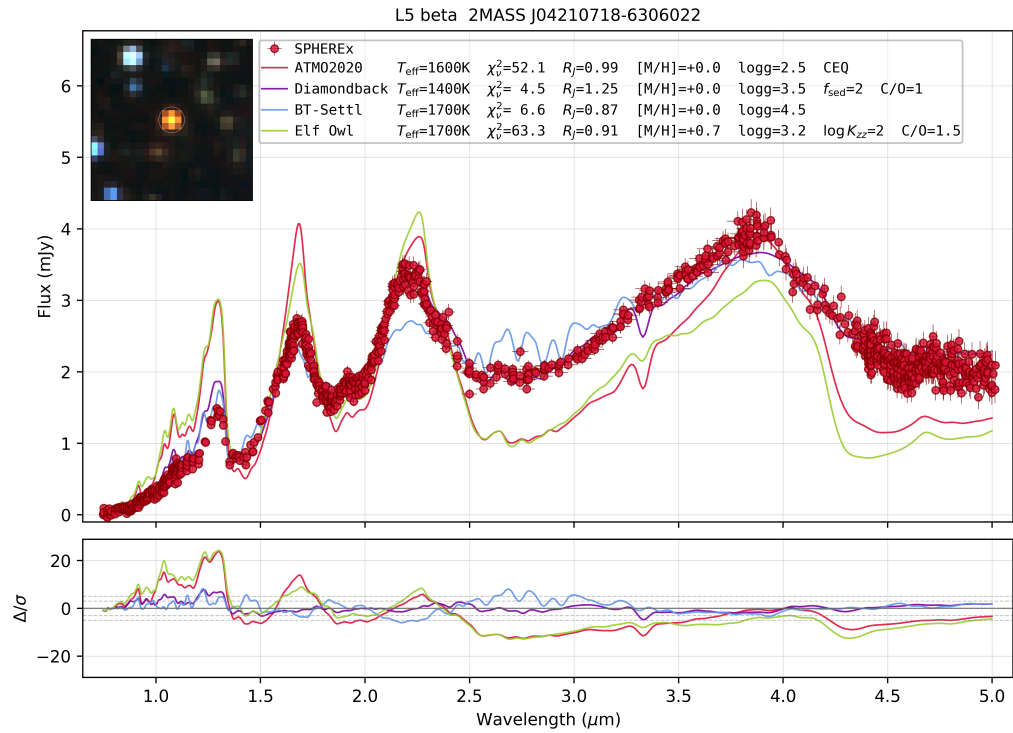


**Figure 18.** Same as Fig. 7, but for the low-gravity L5 $\beta$  dwarf 2MASS J04210718-6306022.

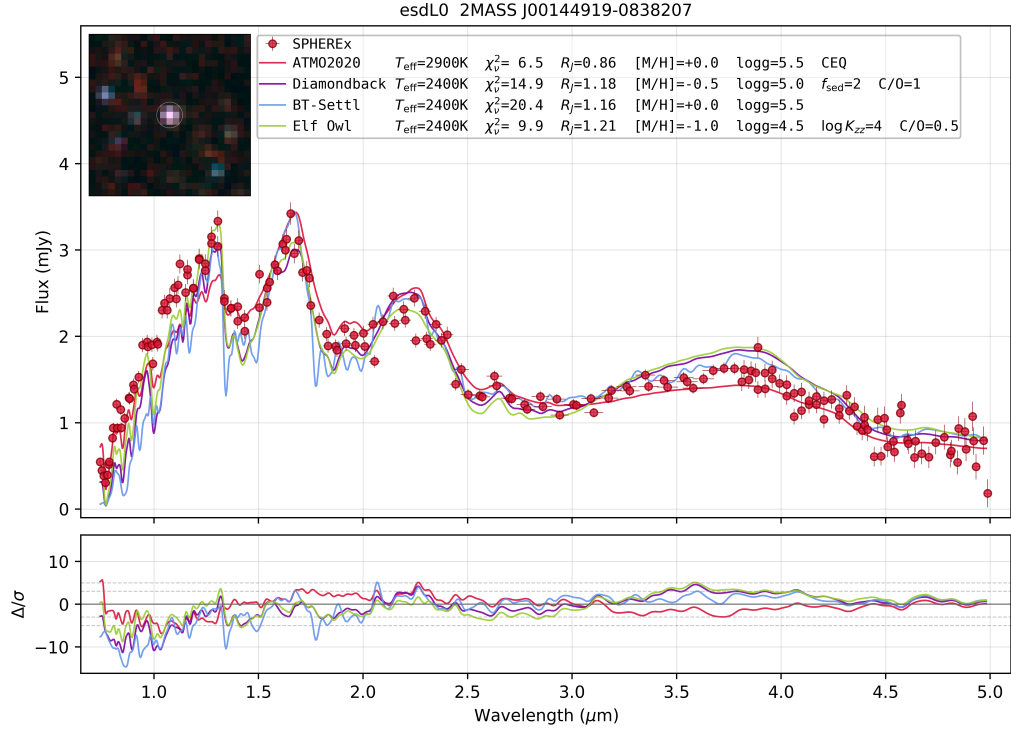


Figure 19. Same as Fig. 7, but for the low metallicity esdL0 dwarf 2MASS J00144919-0838207.

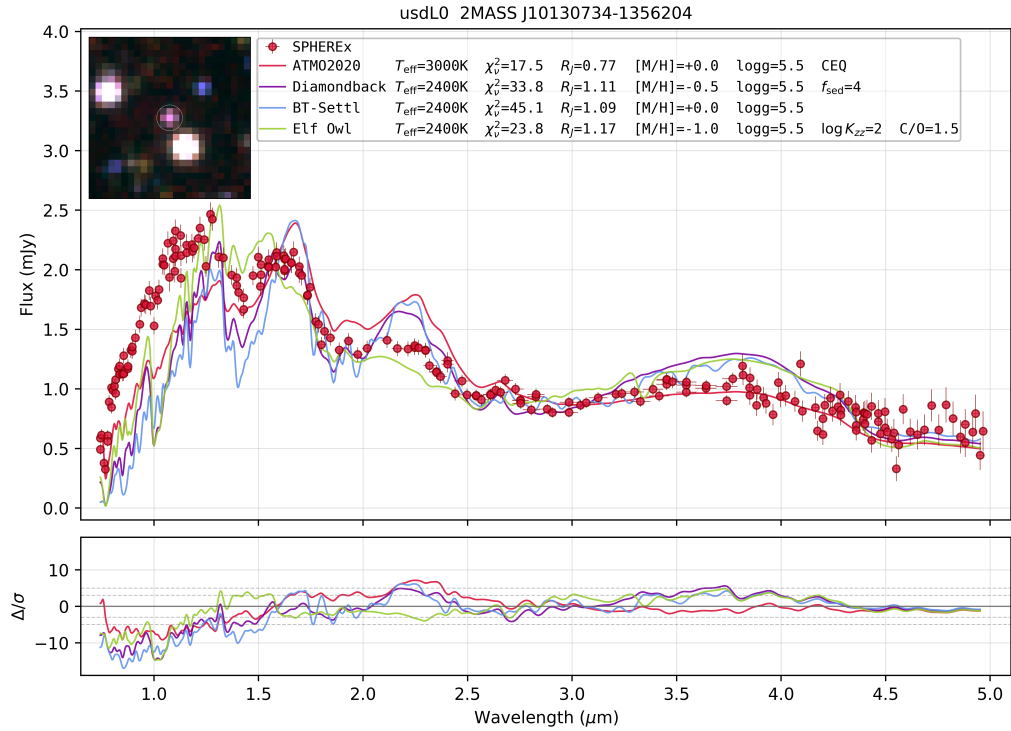


Figure 20. Same as Fig. 7, but for the ultra low metallicity usdL0 dwarf 2MASS J10130734-1356204.

- Gagné, J., Faherty, J. K., Diaz, A. R., et al. 2026, A SPHEREx Pipeline and Spectral Library for Ultracool Dwarfs, <https://arxiv.org/abs/2604.22012>
- Gao, P., Thorngren, D. P., Lee, E. K. H., et al. 2020, *Nature Astronomy*, 4, 951, doi: [10.1038/s41550-020-1114-3](https://doi.org/10.1038/s41550-020-1114-3)
- Gray, R. O., & Corbally, J., C. 2009, *Stellar Spectral Classification*
- Kirkpatrick, J. D. 2005, *ARA&A*, 43, 195, doi: [10.1146/annurev.astro.42.053102.134017](https://doi.org/10.1146/annurev.astro.42.053102.134017)
- Kirkpatrick, J. D., Henry, T. J., & McCarthy, Jr., D. W. 1991, *ApJS*, 77, 417, doi: [10.1086/191611](https://doi.org/10.1086/191611)
- Kirkpatrick, J. D., Reid, I. N., Liebert, J., et al. 1999, *ApJ*, 519, 802, doi: [10.1086/307414](https://doi.org/10.1086/307414)
- Kirkpatrick, J. D., Looper, D. L., Burgasser, A. J., et al. 2010, *ApJS*, 190, 100, doi: [10.1088/0067-0049/190/1/100](https://doi.org/10.1088/0067-0049/190/1/100)
- Kirkpatrick, J. D., Gelino, C. R., Cushing, M. C., et al. 2012, *ApJ*, 753, 156, doi: [10.1088/0004-637X/753/2/156](https://doi.org/10.1088/0004-637X/753/2/156)
- Kirkpatrick, J. D., Gelino, C. R., Faherty, J. K., et al. 2021, *ApJS*, 253, 7, doi: [10.3847/1538-4365/abd107](https://doi.org/10.3847/1538-4365/abd107)
- Kirkpatrick, J. D., Marocco, F., Gelino, C. R., et al. 2024, *ApJS*, 271, 55, doi: [10.3847/1538-4365/ad24e2](https://doi.org/10.3847/1538-4365/ad24e2)
- Kornigut, P. et al. 2026 in prep.
- Kothari, H., Cushing, M. C., Burningham, B., et al. 2024, *ApJ*, 971, 121, doi: [10.3847/1538-4357/ad583b](https://doi.org/10.3847/1538-4357/ad583b)
- Leggett, S. K., & Tremblin, P. 2023, *ApJ*, 959, 86, doi: [10.3847/1538-4357/acfdad](https://doi.org/10.3847/1538-4357/acfdad)
- Leggett, S. K., & Tremblin, P. 2024, *Research Notes of the American Astronomical Society*, 8, 13, doi: [10.3847/2515-5172/ad1b61](https://doi.org/10.3847/2515-5172/ad1b61)
- Leggett, S. K., Tremblin, P., Esplin, T. L., Luhman, K. L., & Morley, C. V. 2017, *ApJ*, 842, 118, doi: [10.3847/1538-4357/aa6fb5](https://doi.org/10.3847/1538-4357/aa6fb5)
- Lépine, S., Rich, R. M., & Shara, M. M. 2007, *ApJ*, 669, 1235, doi: [10.1086/521614](https://doi.org/10.1086/521614)
- Line, M. R., Marley, M. S., Liu, M. C., et al. 2017, *ApJ*, 848, 83, doi: [10.3847/1538-4357/aa7ff0](https://doi.org/10.3847/1538-4357/aa7ff0)
- Lodders, K., & Fegley, B. 2002, *Icarus*, 155, 393, doi: [10.1006/icar.2001.6740](https://doi.org/10.1006/icar.2001.6740)
- Lothringer, J. D., Lowson, N., & Fu, G. 2026, *AJ*, 171, 31, doi: [10.3847/1538-3881/ae1b8e](https://doi.org/10.3847/1538-3881/ae1b8e)
- Lothringer, J. D., Zhou, Y., Apai, D., et al. 2024, *ApJ*, 968, 126, doi: [10.3847/1538-4357/ad43da](https://doi.org/10.3847/1538-4357/ad43da)
- Lueber, A., Kitzmann, D., & Heng, K. 2026, *A&A*, 707, A92, doi: [10.1051/0004-6361/202556207](https://doi.org/10.1051/0004-6361/202556207)
- Marley, M. S., Saumon, D., Visscher, C., et al. 2021, *ApJ*, 920, 85, doi: [10.3847/1538-4357/ac141d](https://doi.org/10.3847/1538-4357/ac141d)
- Morgan, W. W., Keenan, P. C., & Kellman, E. 1943, *An atlas of stellar spectra, with an outline of spectral classification*
- Morley, C. V., Mukherjee, S., Marley, M. S., et al. 2024, *ApJ*, 975, 59, doi: [10.3847/1538-4357/ad71d5](https://doi.org/10.3847/1538-4357/ad71d5)
- Mukherjee, S., Batalha, N. E., Fortney, J. J., & Marley, M. S. 2023, *ApJ*, 942, 71, doi: [10.3847/1538-4357/ac9f48](https://doi.org/10.3847/1538-4357/ac9f48)
- Mukherjee, S., Fortney, J. J., Morley, C. V., et al. 2024, *ApJ*, 963, 73, doi: [10.3847/1538-4357/ad18c2](https://doi.org/10.3847/1538-4357/ad18c2)
- Patten, B. M., Stauffer, J. R., Burrows, A., et al. 2006, *ApJ*, 651, 502, doi: [10.1086/507264](https://doi.org/10.1086/507264)
- Petrus, S., Whiteford, N., Patapis, P., et al. 2024, *ApJL*, 966, L11, doi: [10.3847/2041-8213/ad3e7c](https://doi.org/10.3847/2041-8213/ad3e7c)
- Phillips, M. W., Liu, M. C., & Zhang, Z. 2024, *ApJ*, 961, 210, doi: [10.3847/1538-4357/ad06ba](https://doi.org/10.3847/1538-4357/ad06ba)
- Phillips, M. W., Tremblin, P., Baraffe, I., et al. 2020, *A&A*, 637, A38, doi: [10.1051/0004-6361/201937381](https://doi.org/10.1051/0004-6361/201937381)
- Reiners, A., & Basri, G. 2008, *ApJ*, 684, 1390, doi: [10.1086/590073](https://doi.org/10.1086/590073)
- Rossow, W. B. 1978, *Icarus*, 36, 1, doi: [10.1016/0019-1035\(78\)90072-6](https://doi.org/10.1016/0019-1035(78)90072-6)
- Sanghi, A., Liu, M. C., Best, W. M. J., et al. 2023, *ApJ*, 959, 63, doi: [10.3847/1538-4357/acff66](https://doi.org/10.3847/1538-4357/acff66)
- Saumon, D., Bergeron, P., Lunine, J. I., Hubbard, W. B., & Burrows, A. 1994, *ApJ*, 424, 333, doi: [10.1086/173892](https://doi.org/10.1086/173892)
- Saumon, D., & Marley, M. S. 2008, *ApJ*, 689, 1327, doi: [10.1086/592734](https://doi.org/10.1086/592734)
- Saumon, D., Marley, M. S., Cushing, M. C., et al. 2006, *ApJ*, 647, 552, doi: [10.1086/505419](https://doi.org/10.1086/505419)
- Schneider, A. C., Hardegree-Ullman, K. K., Cushing, M. C., Kirkpatrick, J. D., & Shkolnik, E. L. 2018, *AJ*, 155, 238, doi: [10.3847/1538-3881/aabfc2](https://doi.org/10.3847/1538-3881/aabfc2)
- Sing, D. K., Rustamkulov, Z., Thorngren, D. P., et al. 2024, *Nature*, 630, 831, doi: [10.1038/s41586-024-07395-z](https://doi.org/10.1038/s41586-024-07395-z)
- Skrutskie, M. F., Cutri, R. M., Stiening, R., et al. 2006, *AJ*, 131, 1163, doi: [10.1086/498708](https://doi.org/10.1086/498708)
- SPHEREx Team. 2025, SPHEREx Quick Release Spectral Images - QR2, IPAC, doi: [10.26131/IRSA652](https://doi.org/10.26131/IRSA652)
- Stephens, D. C., Leggett, S. K., Cushing, M. C., et al. 2009, *ApJ*, 702, 154, doi: [10.1088/0004-637X/702/1/154](https://doi.org/10.1088/0004-637X/702/1/154)
- Suárez, G., & Metchev, S. 2022, *MNRAS*, 513, 5701, doi: [10.1093/mnras/stac1205](https://doi.org/10.1093/mnras/stac1205)
- Suárez, G., Metchev, S., Leggett, S. K., Saumon, D., & Marley, M. S. 2021, *ApJ*, 920, 99, doi: [10.3847/1538-4357/ac1418](https://doi.org/10.3847/1538-4357/ac1418)
- Tannock, M. E., Metchev, S., Hood, C. E., et al. 2022, *MNRAS*, 514, 3160, doi: [10.1093/mnras/stac1412](https://doi.org/10.1093/mnras/stac1412)
- Tu, Z., Wang, S., Huang, H., Chen, X., & Liu, J. 2026, SPHEREx Ultracool Dwarf spectral Atlas (SUDA): Atmospheric and Fundamental Parameters of Ultracool Dwarfs, <https://arxiv.org/abs/2604.26771>
- Vos, J. M., Biller, B. A., Allers, K. N., et al. 2020, *AJ*, 160, 38, doi: [10.3847/1538-3881/ab9642](https://doi.org/10.3847/1538-3881/ab9642)

Wright, E. L., Eisenhardt, P. R. M., Mainzer, A. K., et al.  
2010, *AJ*, 140, 1868, doi: [10.1088/0004-6256/140/6/1868](https://doi.org/10.1088/0004-6256/140/6/1868)

Zhang, Z., Liu, M. C., Marley, M. S., Line, M. R., & Best,  
W. M. J. 2021, *ApJ*, 916, 53,  
doi: [10.3847/1538-4357/abf8b2](https://doi.org/10.3847/1538-4357/abf8b2)  
Zhang, Z. H., Pinfield, D. J., Gálvez-Ortiz, M. C., et al.  
2017, *MNRAS*, 464, 3040, doi: [10.1093/mnras/stw2438](https://doi.org/10.1093/mnras/stw2438)